J. metamorphic Geol., 2006, **24,** 193–217 doi:10.1111/j.1525-1314.2006.00633.x

Dating metamorphic reactions and fluid flow: application to exhumation of high-*P* granulites in a crustal-scale shear zone, western Canadian Shield

K. H. MAHAN,[1,*] P. GONCALVES,[2] M. L. WILLIAMS[1] AND M. J. JERCINOVIC[1]
[1]*Department of Geosciences, University of Massachusetts-Amherst, 611 N. Pleasant St., Amherst, MA 01003, USA (kmahan@gps.caltech.edu)*
[2]*Department of Geosciences, University of Franche-Comté, 16 route de Gray, 25030 Besançon, France*

ABSTRACT The Legs Lake shear zone is a crustal-scale thrust fault system in the western Canadian Shield that juxtaposes high-pressure (1.0+ GPa) granulite facies rocks against shallow crustal (< 0.5 GPa) amphibolite facies rocks. Hangingwall decompression is characterized by breakdown of the peak assemblage Grt + Sil + Kfs + Pl + Qtz into the assemblage Grt + Crd + Bt ± Sil + Pl + Qtz. Similar felsic granulite occurs throughout the region, but retrograde cordierite is restricted to the immediate hangingwall of the shear zone. Textural observations, petrological analysis using P–T/P–M_{H_2O} phase diagram sections, and *in situ* electron microprobe monazite geochronology suggest that decompression from peak conditions of 1.1 GPa, *c.* 800 °C involved several distinct stages under first dry and then hydrated conditions. Retrograde re-equilibration occurred at 0.5–0.4 GPa, 550–650 °C. Morphology, X-ray maps, and microprobe dates indicate several distinct monazite generations. Populations 1 and 2 are relatively high yttrium (Y) monazite that grew at 2.55–2.50 Ga and correspond to an early granulite facies event. Population 3 represents episodic growth of low Y monazite between 2.50 and 2.15 Ga whose general significance is still unclear. Population 4 reflects low Y monazite growth at 1.9 Ga, which corresponds to the youngest period of high-pressure metamorphism. Finally, population 5 is restricted to the hydrous retrograded granulite and represents high Y monazite growth at 1.85 Ga that is linked directly to the synkinematic garnet-consuming hydration reaction (KFMASH): Grt + Kfs + H_2O = Bt + Sil + Qtz. Two samples yield weighted mean microprobe dates for this population of 1853 ± 15 and 1851 ± 9 Ma, respectively. Subsequent xenotime growth correlates with the reaction: Grt + Sil + Qtz + H_2O = Crd. We suggest that the shear zone acted as a channel for fluid produced by dehydration of metasediments in the underthrust domain.

Key words: felsic granulite; lower crust; monazite; shear zones; Snowbird tectonic zone.

INTRODUCTION

Interactions between deformation, fluid flow and metamorphism encompass a large variety of interdependent processes. For example, rock deformation can help overcome kinetic barriers to metamorphic reactions (e.g. Vernon, 1976; Yund & Tullis, 1991) and commonly results in enhanced permeability, which can lead to channelization of fluid flow within regions of heterogeneous strain (e.g. Etheridge *et al.*, 1983; Selverstone *et al.*, 1991; Oliver, 1996). In turn, combined deformation and fluid infiltration may profoundly influence metamorphic assemblages, bulk geochemistry and mass transfer, all of which can influence how subsequent deformation is accommodated. Metamorphic reactions induce changes in volume and rheological properties and therefore affect the nature of active deformation mechanisms (e.g. Etheridge *et al.*, 1983; Glazner & Bartley, 1991; Selverstone *et al.*, 1991; Guiraud *et al.*, 2001; Barnes *et al.*, 2004). Understanding these interactions is critical for models of the behaviour, tectonic history and evolution of the continental crust.

Ductile shear zones can provide excellent opportunities to investigate the relationships between deformation, fluid flow and metamorphic reactions. Critical elements in these investigations involve determining the relative and absolute timing of fabric development, metamorphic assemblages and reactions, and changes in fluid abundance and composition. While many studies have established indirect links between fluid flow and active shear zones (e.g. by correlating the dates of shearing with separately determined ages of fluid-producing metamorphism or fluid-related alteration, Barnes *et al.*, 2004; Clark *et al.*, 2005), we establish a more direct link between

**Present address*: K. H. Mahan, Division of Geological and Planetary Sciences, California Institute of Technology, Mailstop 100-23, Pasadena, CA 91125, USA.

these processes by dating synkinematic metamorphic reactions that required and consumed infiltrated fluid.

While the potential for directly dating metamorphism and deformation processes with accessory phases such as monazite and titanite has been recognized for some time (e.g. Parrish, 1990; Gromet, 1991), more recent studies have highlighted the potential complexity of accessory phase growth histories. Recent studies have correlated monazite growth with major prograde reactions in pelitic (e.g. andalusite, garnet, staurolite and sillimanite isograds; Pyle & Spear, 2003; Wing *et al.* 2003; Gibson *et al.*, 2004; Kohn & Malloy, 2004) and calc-alkaline igneous bulk compositions (e.g. Bingen & van Breemen, 1998). Similarly, some retrograde silicate reactions have also been shown to result in monazite growth (Pyle & Spear, 2003; Goncalves *et al.*, 2004; Paquette *et al.*, 2004; McFarlane *et al.*, 2005; this study). It is clear that multiple monazite growth episodes can occur during a single metamorphic cycle, and thus it is critical to improve both our understanding of links between major and accessory phase petrogenesis and the ability to distinguish and date poly-episodic geochronometers on the scale of individual grains.

Here, we focus on the retrograde evolution of high-pressure (high-*P*), granulite facies gneiss in the hangingwall of a major Proterozoic thrust-sense ductile shear zone in the western Canadian Shield. The retrograde metamorphic and hydration processes that affected the initially anhydrous assemblage in felsic granulite (Grt–Sil–Kfs–Pl–Qtz) are modelled via *P–T* and P–M_{H_2O} phase diagram sections (i.e. pseudosections). The microstructures of the reactant and product phases are used to determine the relative timing of specific reactions with respect to shear zone deformation and fluid infiltration. From textural setting, morphology and composition, five monazite populations are distinguished. The first four populations reflect the earlier history of the region, prior to shear zone initiation, whereas the fifth population of monazite, consisting of < 15 μm wide rims, along with late apatite and xenotime crystallization, are linked directly to synkinematic retrograde hydration reactions involving the breakdown of garnet. The monazite populations are dated using electron microprobe (EMP) Th–U–Pb geochronology, a technique having the advantages of both *in situ* analytical capability and high spatial resolution (Suzuki *et al.*, 1991; Montel *et al.*, 1996; Williams & Jercinovic, 2002; Jercinovic & Williams, 2005; Pyle *et al.*, 2005). The result is an improved understanding of fluid infiltration and metamorphic reactions during deformation as well as a better sense of the relative timing of these processes with respect to shear zone evolution. The study elucidates critical stages in the exhumation of high-*P* rocks within the hangingwall of the shear zone and also provides important insight into the earlier polymetamorphic history of those rocks.

GEOLOGICAL BACKGROUND

East Lake Athabasca region

The east Lake Athabasca region (Fig. 1) is a large exposure ($> 20\,000$ km^2) of high-*P* granulite facies

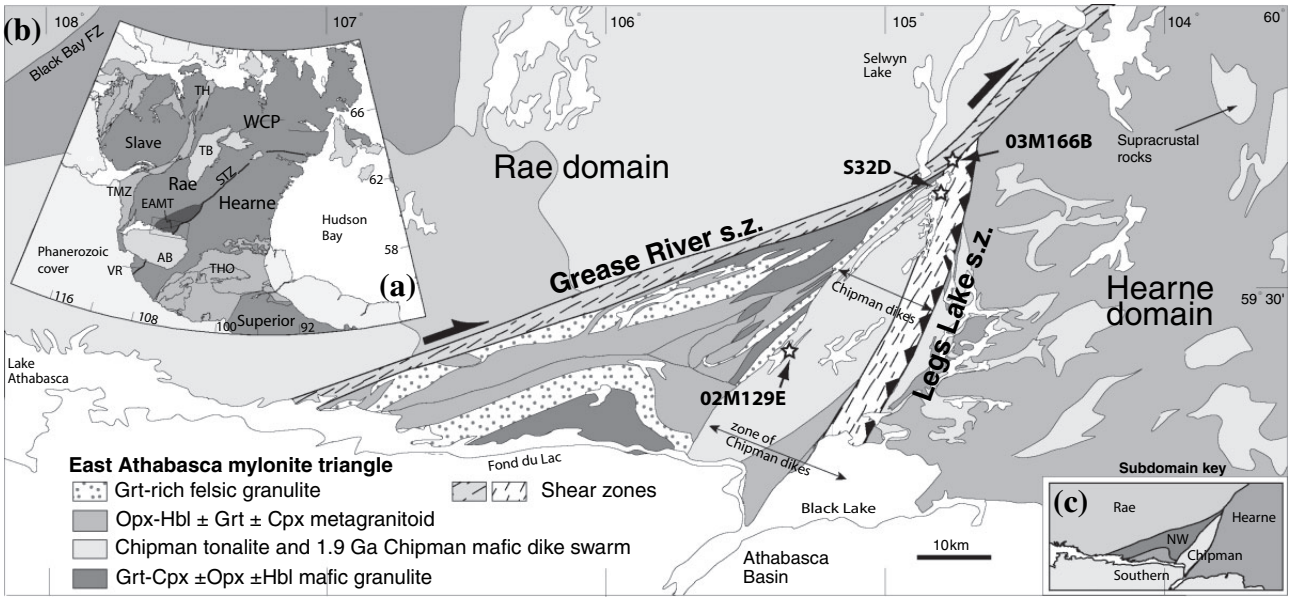

Fig. 1. (a) Simplified map of western Canadian Shield. Dark shaded area-east Lake Athabasca region; AB, Athabasca basin; STZ, Snowbird tectonic zone; TMZ, Taltson magmatic zone; TH, Thelon orogen; THO, Trans-Hudson Orogen; TB, Thelon basin; WCP, Western Churchill Province. (b) Geological map of the East Athabasca mylonite triangle and surrounding Rae and Hearne domains. Note that most workers consider the East Athabasca mylonite triangle to be part of the Rae domain. The locations of three samples are shown with stars. East Athabasca mylonite triangle geology after Hanmer (1997). (c) Key to major lithotectonic subdomains of the East Athabasca mylonite triangle.

rocks (e.g. Williams & Hanmer, 2005). The region's south-eastern boundary is the central segment of the Snowbird tectonic zone, the *c*. 3000 km long, geophysically defined boundary between the Rae and Hearne domains (Fig. 1a) (Hoffman, 1988). In this region, the Snowbird tectonic zone corresponds to a major structural and metamorphic discontinuity, the Legs Lake shear zone, that juxtaposes high-*P* rocks (> 1.0+ GPa) against supracrustal rocks of low- to mid-pressure amphibolite facies (< 0.5 GPa) belonging to the Hearne domain (Mahan *et al*., 2003; Mahan & Williams, 2005).

In the east Lake Athabasca region, the Rae domain consists of dominantly tonalitic gneiss, orthopyroxene-bearing meta-granitoid, meta-gabbro and felsic granulite. The most extensively studied portion was called the East Athabasca mylonite triangle by Hanmer *et al*. (1994) and Hanmer (1997) and is divided into three lithotectonic subdomains: southern, north-western and Chipman (Fig. 1c). Protolith igneous ages range from *c*. 3.0 to 2.6 Ga (Hanmer, 1997). More detailed descriptions of the lithological distribution, high-grade metamorphic characteristics and geochronology are given in Snoeyenbos *et al*. (1995), Williams *et al*. (1995, 2000), Hanmer (1997), Kopf (1999), Krikorian (2002), Baldwin *et al*. (2003, 2004), Flowers *et al*. (in press), and Williams & Hanmer (2005). Two periods of high-*P* granulite facies tectonometamorphism are recorded. The first occurred in the late Archean between *c*. 2.6 and 2.5 Ga (Hanmer, 1997; Williams *et al*., 2000; Flowers, 2005). Archean rocks were subsequently overprinted in the Early Proterozoic (Williams *et al*., 1995, 2000; Kopf, 1999; Krikorian, 2002; Baldwin *et al*., 2003, 2004; Flowers *et al*., in press). Locally, in the southern subdomain, very high-*P* (> 1.5 GPa, 900 °C) assemblages in mafic granulite and eclogite have been documented (Snoeyenbos *et al*., 1995; Baldwin *et al*., 2003, 2004) with metamorphic zircon precisely dated by thermal ionization mass spectrometry (TIMS) at 1904 ±0.9 Ma and 1904 ±0.3 Ma, respectively (Baldwin *et al*., 2003, 2004). The region was subsequently affected by intense high-*P* metamorphism (*c*. 1.1–1.0 GPa, 750–850 °C) that is temporally best constrained by a TIMS date of 1896 ± 0.3 Ma for metamorphic zircon in partially melted mafic dykes (Flowers *et al*., in press). Final regional exhumation must have occurred prior to deposition of sediments in the overlying *c*. 1.7 Ga Athabasca basin (Fig. 1a,b) (Rayner *et al*., 2003).

Legs Lake and Grease River shear zones

Two major post-1.9 Ga ductile shear zones significantly influenced the present-day distribution of high-*P* rocks in the east Lake Athabasca region (Mahan *et al*., 2003; Mahan & Williams, 2005). First, the Legs Lake shear zone marks the structural and metamorphic boundary between the deep-crustal (1.0+ GPa) Rae and the shallow-crustal (< 0.5 GPa) Hearne domains. The structure is correlated with along-strike faults that combine to make a *c*. 500 km long contractional system (Mahan & Williams, 2005). In the east Lake Athabasca region, the shear zone consists of a 5–8 km wide northwest-dipping zone of intense amphibolite facies deformation that records east-vergent thrusting (Fig. 1b) (Mahan *et al*., 2003). The magnitude of juxtaposition across the Legs Lake shear zone (at least 20 vertical kilometres) suggests regional-scale uplift of the high-*P* terrane and indicates that the shear zone played a fundamental role in the regional exhumation history. Prograde metamorphism in the footwall (i.e. Hearne domain), which is characterized by early passage through andalusite stability and peaked at < 0.5 GPa and 600 °C, coincided with shear zone deformation (Mahan *et al*., 2003). Monazite (EMP and TIMS) and zircon (TIMS) geochronology from the shear zone, including data presented here, suggest that deformation in the shear zone and prograde metamorphism in the Hearne province occurred during the interval of 1850–1800 Ma, coincident with collisional events in the Trans-Hudson orogeny to the south-east (Fig. 1a) (Mahan & Williams, 2005).

Second, the Grease River shear zone is a *c*. 400 km long east–northeast trending, dextral strike–slip structure that extends from the south-west, where it is concealed beneath the Athabasca basin, across the east Lake Athabasca region and into the Hearne domain (Slimmon, 1989; Card, 2001; Mahan & Williams, 2005). In the east Lake Athabasca region, the shear zone is a several kilometre-wide zone of amphibolite to greenschist facies and ductile-brittle tectonite (Fig. 1). Strike–slip deformation within the Grease River shear zone overprints and offsets the north-eastern extension of the Legs Lake shear zone by *c*. 110 km (Mahan & Williams, 2005). A preliminary 1788 +28/−15 Ma crystallization age (zircon by TIMS) for a late-syn-kinematic granite dyke (Hanmer, 1997) and *c*. 1.80 Ga syn-kinematic EMP monazite dates (Williams & Jercinovic, 2002) indicate a *c*. 1.80–1.79 Ga age for the shear zone.

PETROGRAPHY, MICROSTRUCTURE AND MINERAL COMPOSITIONS

Leucocratic garnetiferous felsic granulite occupies a substantial portion of the east Lake Athabasca region. Within the East Athabasca mylonite triangle (Fig. 1b), the majority of this rock occurs in the north-western and southern subdomains (Hanmer *et al*., 1994), but numerous relatively narrow screens (metres to tens of metres wide) of similar rock crop out within the Chipman domain, west of and within the Legs Lake shear zone (Fig. 1b).

The felsic granulite in the southern subdomain is characterized by the mineral association Grt + ternary fsp + Qtz + Ky + Rt (abbreviations after Kretz, 1983 and Bucher & Frey, 2002) and has been described in detail by Snoeyenbos *et al*. (1995) and

Baldwin *et al.* (in press). This granulite differs from that in the north-western and Chipman subdomains mainly by the occurrence of kyanite and ternary feldspar, which is now exsolved to K-feldspar and plagioclase (Snoeyenbos *et al.*, 1995). The co-existence of kyanite and temperatures of 1000 °C, calculated using feldspar re-homogenization thermometry, led Snoeyenbos *et al.* (1995) to suggest that the southern subdomain reached > 1.5 GPa conditions. Although Baldwin *et al.* (in press) suggest that kyanite and ternary feldspar may have never been in equilibrium in the felsic granulite, detailed studies of mafic lithologies in the area (Baldwin *et al.*, 2003, 2004) are consistent with a generally higher pressure and temperature history for that subdomain *v.* the north-western and Chipman subdomains. Because the tectonic significance of apparent disparities in high-grade *P–T* history between these subdomains is not yet well understood and beyond the scope of this paper, and because only the Chipman subdomain forms the immediate hangingwall of the Legs Lake shear zone in this region, further description/discussion of felsic granulite is restricted to that in the Chipman subdomain unless noted otherwise.

In the Chipman subdomain, the Chipman mafic dyke swarm is interpreted to have intruded all other major units (Hanmer, 1997). These dykes contain the peak assemblage Grt–Cpx–Hbl–Pl–Qtz and were metamorphosed under granulite facies conditions of 750–850 °C, 1.0–1.1 GPa (Williams *et al.*, 1995). Dyke emplacement and metamorphism is interpreted to have occurred almost synchronously at 1896 Ma (Williams *et al.*, 1995; Flowers *et al.*, in press). The host rock to the dykes, including the felsic granulite, is inferred to have experienced similar metamorphic conditions at that time.

Samples of felsic granulite from three structural settings in the Chipman subdomain were studied: (1) an area preserved from the influence of the post-1.9 Ga shear zones where the felsic gneiss displays little evidence for retrograde metamorphism (anhydrous felsic granulite 02M129E), (2) an area within the hangingwall of the Legs Lake shear zone where significant evidence of hydration and retrograde metamorphism occurs (hydrous retrograde felsic granulite S32D), and (3) an area that first experienced Legs Lake deformation and was subsequently overprinted by the younger Grease River shear zone (hydrous retrograde felsic granulite 03M166B) (see sample locations in Fig. 1b).

Analytical methods

All major element analysis and X-ray mapping was performed using a Cameca SX-50 electron microprobe

Table 1. Representative silicate compositions for felsic granulites.

	Anhydrous granulite				Hydrous retrograded granulite											
	02M129E				S32D					03M166B						
	Grt		PI	Kfs	Grt	Crd	Bt matrix	PI		Grt		Crd	Bt matrix	PI	
Oxides	Lower Ca core	Higher Ca rim						Lower Ca core	Higher Ca rim	Higher Ca remnant interior	Lower Ca remnant margin			Higher Ca core	Lower Ca rim
SiO_2	40.32	40.25	63.40	65.42	37.52	48.88	35.47	60.75	59.73	36.62	36.60	48.37	34.47	61.80	63.29
TiO_2	–	–	–	–	0.00	0.00	1.29	–	–	–	–	–	3.67	–	–
Al_2O_3	22.19	22.00	23.28	18.50	21.86	33.94	18.93	25.17	26.00	21.78	21.45	33.59	18.88	24.36	23.49
FeO	24.19	23.96	0.03	0.04	35.82	6.27	20.07	0.17	0.39	34.72	36.76	7.43	19.19	0.00	0.14
MgO	12.93	12.29	–	–	3.95	9.76	13.03	–	–	4.40	3.52	9.08	9.90	–	–
MnO	0.26	0.32	–	–	1.63	0.05	0.01	–	–	1.02	1.19	0.04	0.06	–	–
CaO	0.97	1.32	5.14	0.18	1.13	0.00	0.00	5.97	6.74	1.60	0.84	0.00	0.00	5.53	4.09
Na_2O	–	–	8.78	1.37	–	0.17	0.21	8.83	8.10	–	–	0.14	0.19	8.53	9.46
K_2O	–	–	0.28	14.09	–	0.02	8.46	0.04	0.09	–	–	0.01	9.10	0.05	0.06
Total	100.86	100.15	100.91	99.59	101.91	99.10	97.49	100.92	101.05	100.15	100.36	98.66	95.46	100.28	100.55
Oxygen	12	12	8	8	12	18	11	8	8	12	12	18	11	8	8
Si	3.01	3.03	2.78	3.01	2.96	4.95	2.63	2.68	2.64	2.93	2.95	4.95	2.62	2.73	2.79
Ti	–	–	–	–	0.00	0.00	0.07	–	–	–	–	–	0.21	–	–
Al	1.95	1.95	1.21	1.00	2.03	4.05	1.66	1.31	1.36	2.06	2.04	4.05	1.69	1.27	1.22
Fe	1.51	1.51	0.00	0.00	2.36	0.53	1.25	0.01	0.01	2.32	2.48	0.64	1.22	0.00	0.01
Mg	1.44	1.38	–	–	0.46	1.47	1.44	–	–	0.53	0.42	1.38	1.12	–	–
Mn	0.02	0.02	–	–	0.11	0.01	0.00	–	–	0.07	0.08	0.00	0.00	–	–
Ca	0.08	0.11	0.24	0.01	0.10	0.00	0.00	0.28	0.32	0.14	0.07	0.00	0.00	0.26	0.19
Na	–	–	0.75	0.12	–	0.03	0.03	0.76	0.70	–	–	0.03	0.03	0.73	0.81
K	–	–	0.02	0.83	–	0.00	0.80	0.00	0.01	–	–	0.00	0.88	0.00	0.00
Mg#	0.49	0.48	–	–	0.16	0.74	0.54	–	–	0.18	0.15	0.69	0.48	–	–
Alm	0.50	0.50	–	–	0.78	–	–	–	–	0.76	0.81	–	–	–	–
Prp	0.47	0.46	–	–	0.15	–	–	–	–	0.17	0.14	–	–	–	–
Sps	0.01	0.01	–	–	0.04	–	–	–	–	0.02	0.03	–	–	–	–
Grs	0.025	0.035	–	–	0.03	–	–	–	–	0.05	0.02	–	–	–	–
An	–	–	0.24	0.00	–	–	–	0.27	0.31	–	–	–	–	0.26	0.19
Ab	–	–	0.74	0.13	–	–	–	0.73	0.68	–	–	–	–	0.73	0.80
Kfs	–	–	0.02	0.87	–	–	–	0.00	0.01	–	–	–	–	0.00	0.00

Mg# = $X_{Mg}/X_{Fe} + X_{Mg}$. Analytical conditions: 15 kV,15 nA,20 s(peak), 10 s(background), focused beam. Common silicate standards were used.

at the University of Massachusetts-Amherst, USA. Major element analytical conditions are given in Table 1. X-ray maps of garnet were made using a 200 nA beam current, 45 ms count time, and 10–15 μm step sizes. Concentrations of Y in garnet were measured using a Cameca SX-100 microprobe with all five spectrometers counting on Y Lα using PET and LPET crystals, a 200 nA beam current, 500 s count time, and Y-garnet (YAG) as a standard.

Anhydrous felsic granulite

The ubiquitous peak assemblage preserved in the anhydrous felsic granulite in the Chipman subdomain of the east Lake Athabasca region is Grt + Sil + Kfs + Pl + Qtz with accessory rutile, monazite, zircon and apatite. The gneissic fabric of anhydrous granulite 02M129E (Fig. 2a) is characteristic of that in the area where it was collected and predates the post-1.9 Ga shear zones based on metamorphic grade and kinematic patterns. Pink to lilac garnet typically comprises 20–30% of the rock volume and occurs as relatively equant, subhedral to anhedral porphyroblasts up to several centimetres in diameter (Fig. 2a). Garnet is not significantly zoned in Mg, Fe or Mn ($X_{Mg} = 0.47$–0.48, $X_{Mn} \leq 0.01$), but a small marked increase in the grossular component is apparent near garnet margins (X_{Ca} increases from *c*. 0.025 to 0.035) (Fig. 3). Silicate compositions are listed in Table 1. In felsic granulite from the southern subdomain, a similar core to rim increase in grossular (though larger in magnitude; $X_{Ca} = 0.06$ to 0.15) was noted by Snoeyenbos *et al*. (1995) and Baldwin *et al*. (in press; see their fig. 5a). Garnet in this study also displays a gradual decrease in Y content from cores (range is 200–175 ppm based on multiple traverses) to rims (60–20 ppm) (Fig. 3). Inclusions in garnet are common and consist of abundant coarse anhedral quartz with lesser amounts of prismatic sillimanite, biotite, rutile, monazite and zircon. Ribbons of matrix plagioclase (An_{24}), K-feldspar, quartz and sillimanite define a strong gneissic foliation (Fig. 2a). Biotite is present as a minor retrograde phase in the matrix and in fractures within garnet.

Hydrous retrograded felsic granulite

Hydrous retrograde felsic granulite from the immediate hangingwall of Legs Lake shear zone is represented by samples S32D and 03M166B. Both samples experienced significant deformation and retrogression within the Legs Lake shear zone. Sample 03M166B was subsequently overprinted by deformation in the Grease River shear zone. Both samples are well foliated with relicts of an anhydrous peak assemblage Grt + Sil + Kfs + Pl + Qtz that has undergone extensive fabric reworking and addition of retrograde biotite and cordierite (Figs 2b,c & 4a,b). Elongate monomineralic ribbons of plagioclase, quartz and biotite define the matrix foliation and are interlayered with finer-grained polymineralic lenses of the same phases. Coarse, prismatic grains of porphyroclastic sillimanite (up to several mm) occur locally within the matrix (Fig. 2b). In S32D, garnet is interpreted to have made up *c*. 30% of the rock by volume (see modes in Table 2) from the trace of relict porphyroblasts (up to 15 mm in diameter). Garnet porphyroblasts are characterized by pervasive, closely spaced and subparallel fractures oriented at a high angle to the matrix foliation (Fig. 2b,c). The fractures are filled with cordierite, biotite and locally sillimanite (Fig. 2c). Note that biotite is abundant in the matrix and wraps around relict garnet porphyroblasts whereas cordierite is only present as a replacement phase inside the porphyroblasts (Fig. 4b). Equant morphology of the garnet porphyroblasts in S32D suggests that (1) the fractures did not undergo significant dilation or translation, (2) that retrograde phases replaced garnet instead of filling open fractures, and (3) that significant deformation did not continue after garnet replacement. Assuming no change in volume, at least 60% of the original garnet was consumed and replaced by the retrograde assemblage. Similar replacement textures, indicating extensive biotite and cordierite growth after garnet, occur in sample 03M166B. However, in contrast to relatively equant garnet in S32D, Grt–Crd aggregates in 03M166B invariably occur as highly elongate clusters, parallel to the reworked fabric, with aspect ratios up to 8:1 (Fig. 2d). These observations are consistent with the interpretation that 03M166B was deformed in the Grease River shear zone after initial retrograde garnet replacement.

Garnet is not significantly zoned in major elements on the scale of whole porphyroblasts. However, a gradual core to rim decrease in Y (*c*. 270–200 ppm in cores and 50–20 ppm in rims) is similar to that observed in garnet from the anhydrous granulite (Fig. 4b). Smaller individual garnet remnants, ranging from *c*. 10 to 100 μm in diameter, are generally homogeneous with the following compositions (S32D): $X_{Mg} = 0.15$, $X_{Mn} = 0.04$ and $X_{Ca} = 0.03$ (Table 1). The largest observed garnet remnants (*c*. 150–500 μm) occur in 03M166B and have a noticeable zoning pattern from the interior to edge of individual remnants. Higher Ca and Mg interiors ($X_{Ca} = 0.04$–0.05, $X_{Mg} = 0.16$–0.17; in 03M166B) give way to a distinct but gradual drop to $X_{Ca} = 0.02$–0.03 that begins *c*. 50–100 μm from the margins of each remnant (Fig. 4c,d). Garnet remnants in both samples also commonly display a sharp decrease in Mg# ($X_{Mg}/[X_{Mg} + X_{Fe}]$) and commonly an increase in Mn at the margins, which are interpreted to reflect late Fe–Mg exchange between garnet and other ferromagnesian phases and back-diffusion of Mn during garnet resorption (e.g. Spear, 1993). The lower Ca in smaller remnants and at the margins of larger remnants is interpreted to represent re-equilibration of garnet during the main period of retrograde metamorphism. If the rims represented

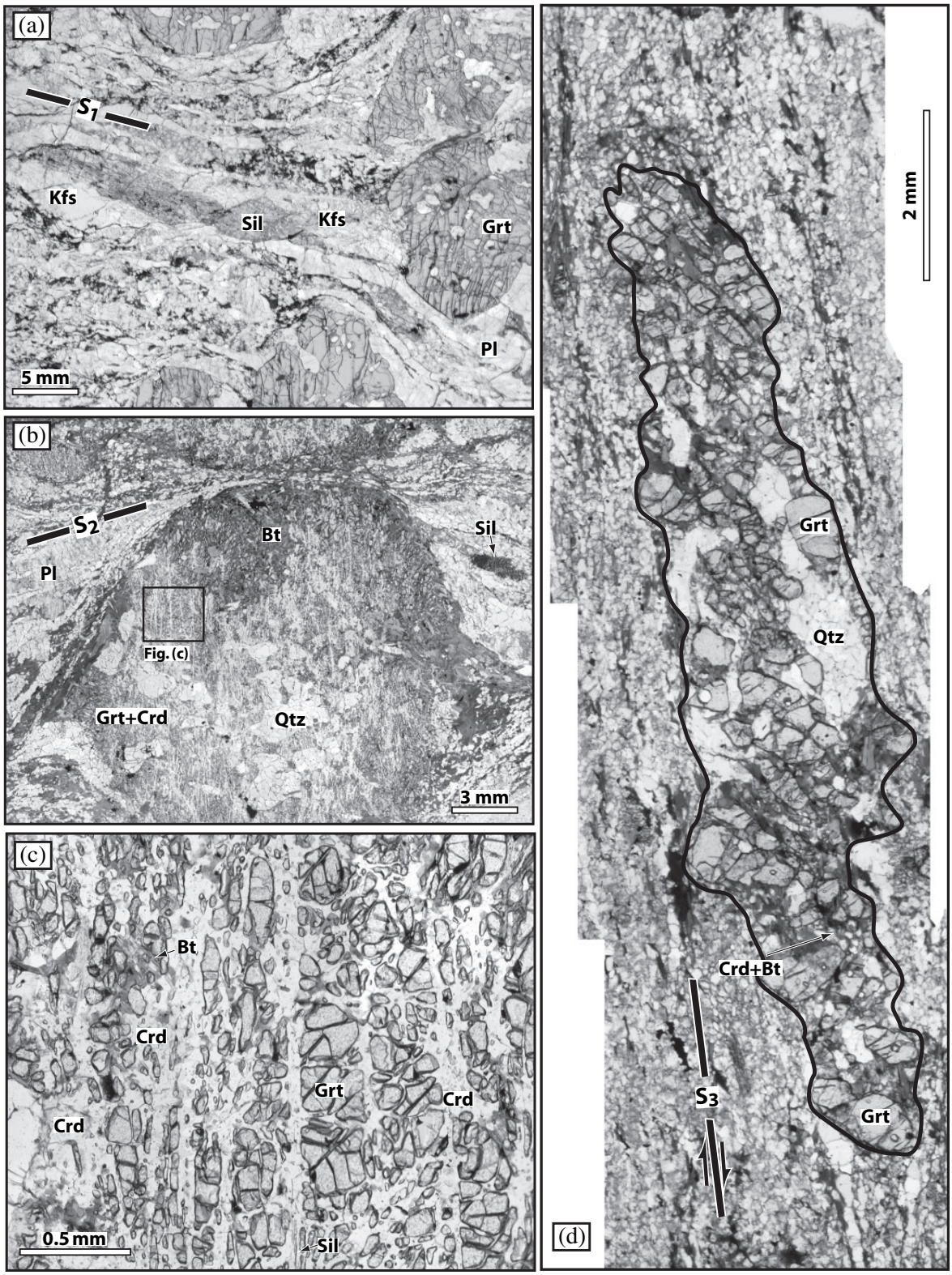

Fig. 2. Photomicrographs. (a) Anhydrous felsic granulite from Cora Lake. S1 refers to the main penetrative deformation fabric in this sample, which predates the Legs Lake shear zone and may itself be a composite fabric. (b) Relict garnet porphyroblast in retrograded felsic granulite S32D. Main fabric is Legs Lake shear zone (S2). (c) Interior of relict garnet porphyroblast in sample S32D. Location shown in (b). (d) Elongate relict garnet porphyroblast in sample 03M166B (margin is outlined). Main fabric (S3) is related to Grease River shear zone.

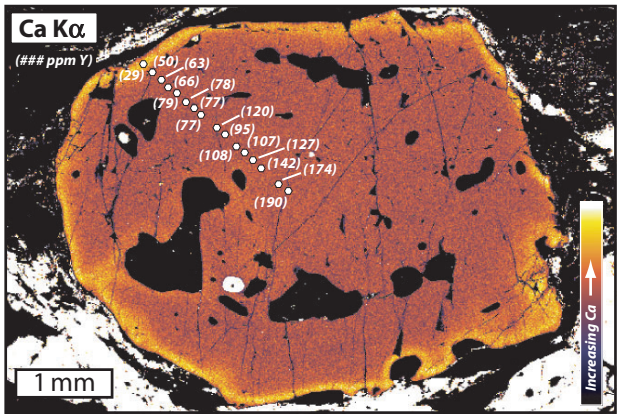

Fig. 3. Ca Kα X-ray map of garnet in anhydrous felsic granulite 02M129E showing marked increase in Ca at garnet margin. Spot locations and Y concentrations in ppm are shown.

Table 2. Modal and bulk compositions.

	Mode	
Phase	02M129E (anhydrous)	S32D (hydrous retrograde)
Modal composition		
Grt	28.8	9.0
Sil	4.4	1.0
Qtz	21.0	28.5
Pl	30.0	29.5
Crd	0.0	8.0
Bt	2.1	24.0
Kfs	13.7	0.0
	Wt %	
Oxide	02M129E (anhydrous)	S32D (hydrous retrograde)
Bulk composition		
FeO	9.4	10.1
MgO	5.1	4.5
CaO	1.7	1.9
Na_2O	2.4	2.4
K_2O	1.9	2.1
Al_2O_3	19.8	17.9
SiO_2	59.6	61.1

garnet growth, a sharp Ca contrast should have been produced rather than the observed gradual change (Fig. 4d). However, late Fe–Mg exchange between garnet, biotite and cordierite is likely to have continued during the cooling history. Therefore, temperatures calculated from Grt–Bt and Grt–Crd equilibria are considered minimum estimates for the temperature of the main phase of retrograde metamorphism.

Matrix plagioclase is slightly zoned to higher Ca at rims in S32D (core-An_{27}, rims-An_{32}) whereas the opposite occurs in 03M166B (cores-An_{25}, rims-An_{19}). Higher Ca in the rims is consistent with growth of new, more anorthitic plagioclase during garnet breakdown. We suggest that lower Ca rim plagioclase in 03M166B is related to dynamic recrystallization during deformation under lower grade metamorphic conditions. Cordierite is not significantly zoned in either sample. The typical Mg# of biotite in S32D and 03M166B is 0.53–0.54 and 0.47–0.48, respectively, but biotite near and among garnet remnants commonly has slightly higher Mg#, probably a reflection of late Fe–Mg exchange.

In summary, garnet in the retrograded felsic granulite appears to have been homogeneous with respect to major elements prior to retrogression. However, higher Ca rims like those observed in the anhydrous felsic granulite may have originally existed but were either largely consumed or re-equilibrated during retrogression. The observed core to rim variation in Y content is interpreted as Rayleigh fractionation type growth zoning (e.g. Pyle & Spear, 1999; Otamendi *et al.*, 2002), and its preservation is likely because of the slow diffusion rate of Y in garnet (e.g. Yang & Rivers, 2002). During major retrogression, smaller garnet remnants were completely re-equilibrated with respect to major elements, including Ca, whereas the interiors of larger remnants preserve Ca content similar to their earlier high-grade(?) composition.

PETROLOGICAL ANALYSIS

Thermobarometry of retrograde conditions

Conventional thermobarometry was not applied to the peak assemblage in the felsic granulite because garnet is the only ferromagnesian phase and therefore no reliable temperature constraint can be obtained. Retrograde conditions were estimated from Bt–Crd–Pl–Grt–Sil–Qtz equilibria. Calculations were performed using both the TWQ 2.02b software of Berman (1991, 1992) and the Thermocalc 3.1.2 Ave-PT method of Powell & Holland (1994) with the internally consistent thermodynamic databases of Berman & Aranovich (1996) and Holland & Powell (1998), respectively. For sample S32D and using the compositions of typical matrix biotite away from garnet, average cordierite and plagioclase, and the interior of the largest garnet remnants (which are < 100 μm) (Table 1), Thermocalc Ave-PT yields 521 ± 122 °C, 0.41 ± 0.14 GPa. This is similar to TWQ estimate for this sample of 575 °C, 0.40–0.43 GPa reported by Mahan *et al.* (2003). For sample 03M166B and using compositions for matrix biotite away from garnet, average cordierite, low Ca marginal plagioclase, and average 'low Ca' marginal garnet from a large remnant (*c.* 400 μm), we calculate 545 ± 130 °C, 0.39 ± 0.14 GPa. As noted in the previous section, these estimates are likely to be minima for the true conditions of main phase retrograde equilibrium.

P–T projection

A *P–T* projection (i.e. petrogenetic grid) and phase diagram sections (i.e. pseudosections) constructed in the system Na_2O–CaO–K_2O–FeO–MgO–Al_2O_3–SiO_2–H_2O (NCKFMASH) were used. Projections and sections were constructed using the software PerpleX_04 (Connolly, 1990; Connolly & Petrini, 2002) and the

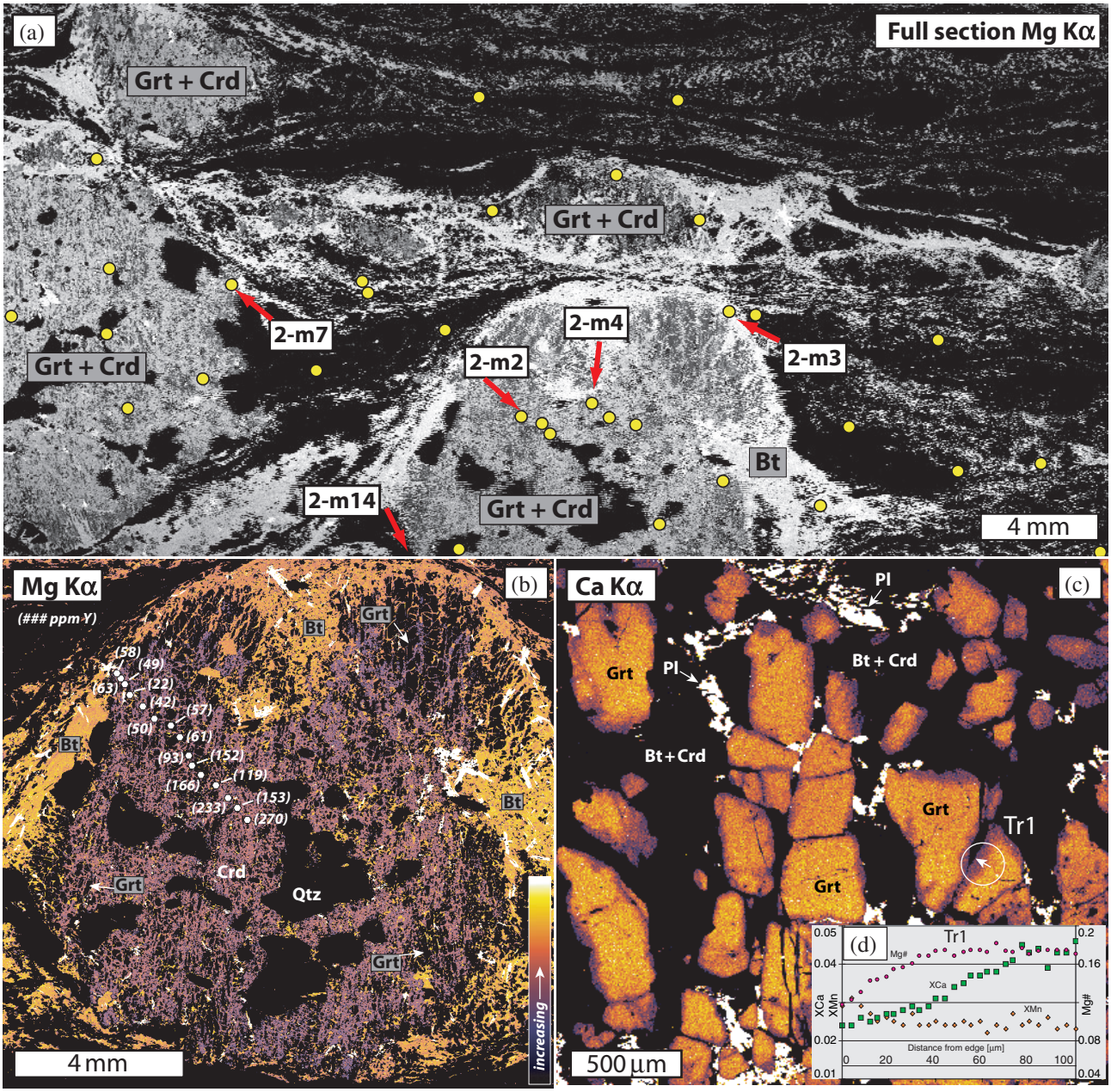

Fig. 4. (a) Mg Kα X-ray map of full thin section from retrograded felsic granulite S32D. Horizontal field of view is 3.5 cm. Lighter colours correspond to higher concentrations of Mg (biotite is white; quartz and plagioclase are black). Yellow circles show the distribution of monazite. Selected monazite grains from which data are reported are labelled. (b) Mg Kα X-ray map of S32D garnet adjusted to show distribution of retrograde biotite (orange/yellow) *v.* cordierite (blue/purple). Note the restriction of cordierite to the interior of garnet porphyroblasts. Minor chlorite (white) is interpreted as a recent retrograde phase that postdates the processes discussed in this study. Spot locations and Y concentrations in ppm are shown. (c) Ca Kα X-ray map of relatively large (up to 500 μm) 'islands' of garnet in relict porphyroblast from retrograded granulite 03M166B. Note the relatively high Ca content in the interior of larger garnet remnants and the dramatic decrease in Ca near all margins *v.* the relatively uniformly low Ca content in smaller islands (e.g. upper right). Location of analytical traverse is shown by white circle. (d) Compositional profile of 100 μm traverse from interior to edge of a garnet remnant in contact with biotite showing gradual decrease in X_{Ca} towards margin. Note also decrease in Mg towards edges and small increase in X_{Mn} at edge.

updated version of the internally consistent thermodynamic database of Holland & Powell (1998). The phases considered are Grt–Opx–Crd–Bt–Spl–Chl–St–Ms–Kfs–And–Sil–Ky–Qtz–H_2O. Solid solution models are given in Table 3.

Phase relations are introduced using a partial *P–T* projection in the sub-system KFMASH (Fig. 5). Relations associated with the [Opx, Ms, St, Chl] invariant point, hereafter referred to as [Opx] for clarity, and the univariant KFMASH reaction:

Table 3. Solution models used for *P–T* projections and sections.

Solution model	Endmembers
Bio(HP)	ann, phl, east, sdph
Gt(HP)	alm, py, gr
Opx(HP)	en, fs, mgts, fets
Pheng(HP)	pa, cel, fcel, mu
hCrd	crd, fcrd, hcrd
Pl(h)	an, abh
Sp(HP)	sp, herc
St(HP)	fst, mst
Chl(HP)	daph, ames, afchl, clin
melt(HP)	foL, faL, silL, anL, h2oL, enL, kspL, diL, abL

See PerpleX documentation (http://www.perplex.ethz.ch) for solution model references and abbreviations used here.

$$\mathrm{Bt + Sil + Qtz = Grt + Crd + Kfs + V} \quad \mathrm{(Opx,Spl)} \quad (1)$$

are of particular interest. The KFASH sub-system consists of four invariant points, defining the stable end-member grid, and one unstable point:]Fs,Hc[. As bulk X_{Mg} increases, the KFASH invariant points become KFMASH pseudo-invariant points (definition from Connolly, 1990), and their positions move along the KFMASH univariant reactions (small grey arrows in Fig. 5). The pseudo-invariant point [Opx,Spl] becomes stable at points beyond the [Opx] invariant point, which corresponds to bulk X_{Mg} of *c.* 0.027. Therefore, for most natural systems including the felsic granulites of this study (bulk X_{Mg} is 0.35–0.42 for our samples), the topology of the pseudo-invariant point [Opx,Spl] and its associated pseudo-univariant curves can be used to place broad qualitative constraints on the *P–T* path that corresponds to the breakdown of a Grt–Sil–Kfs–Qtz peak assemblage into Grt–Bt–Sil–Crd–Qtz. One possibility involves a sequence of KFMASH divariant reactions such as:

$$\mathrm{Grt + Kfs + V = Bt + Sil + Qtz} \quad \mathrm{(Opx,Spl,Crd)} \quad (2)$$

followed by the degenerate reaction

$$\mathrm{Grt + Sil + Qtz + V = Crd} \quad \mathrm{(Opx,Spl,Kfs,Bt)} \quad (3)$$

along a cooling and decompression path (Fig. 5). Because the KFMASH univariant reaction (1) is stable over a wide *P–T* range, the associated divariant reactions (2) and (3) are potentially applicable over a very large pressure range (up to 1.4 GPa).

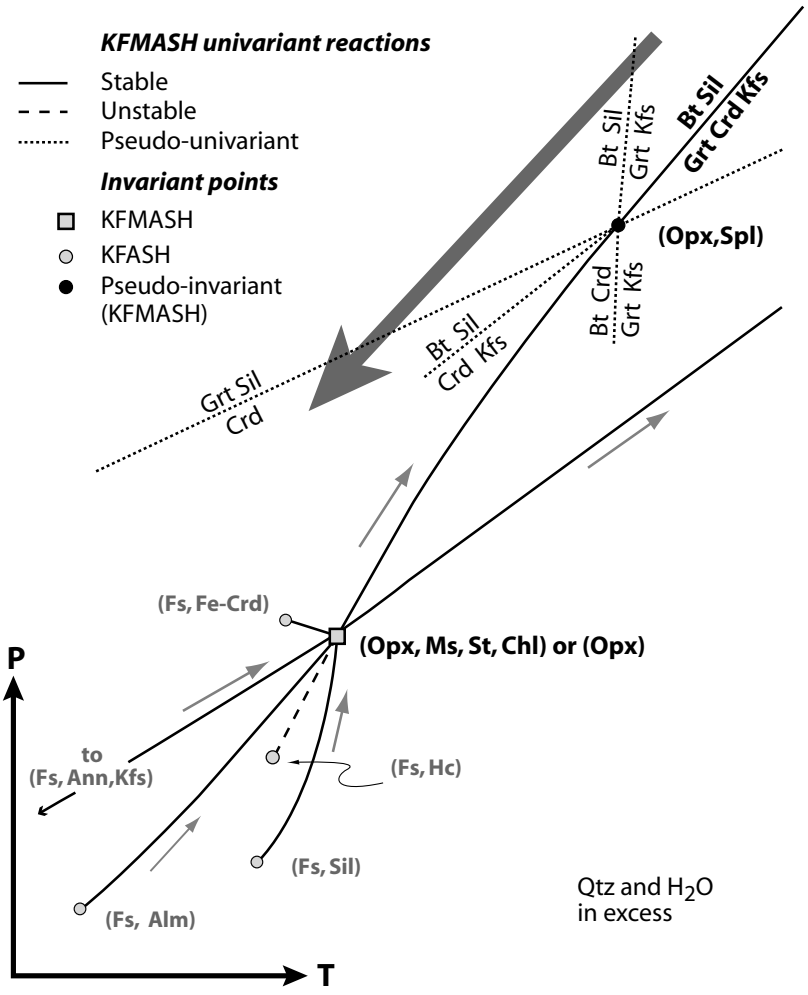

Fig. 5. KFASH–KFMASH partial grid. Light grey arrows mark the direction that KFMASH pseudoinvariant points move with increasing bulk X_{Mg}. Heavy grey arrow represents possible retrograde *P–T* path.

P–T phase diagram sections

A major assumption in the qualitative *P–T* path segment shown in Fig. 5 is that this evolution occurred under persistent fluid-saturated conditions, which is not possible given that the peak assemblage is anhydrous. Therefore, phase diagram sections, constructed for specific bulk compositions were used, to quantitatively evaluate the dependence of mineral assemblage on variations in pressure, temperature and quantity of fluid (M_{H_2O}).

The bulk compositions used to construct the sections were calculated via a combination of major phase mode estimation from X-ray maps and digital image analysis (Table 2) and the mineral compositions (Table 1). The bulk compositions determined for the anhydrous (02M129E) and hydrous retrograde (S32D) granulite samples are similar to one another and are within the range of whole-rock compositions determined by XRF for well-preserved anhydrous felsic granulite in other parts of the east Lake Athabasca region (Baldwin, 2003; Flowers, 2005). We do not consider bulk compositional effects because of crystal fractionation during garnet growth, which has been shown by many workers to be significant for low to medium temperature (*c.* < 700 °C peak *T*) metamorphic rocks (e.g. Evans, 2004), and assume that all garnet contributed to the effective bulk composition.

Figure 6(a) shows a *P–T* pseudosection calculated for the anhydrous felsic granulite 02M129E composition in the system NCKFMAS. The position of the solidus shows that most of the phase diagram is stable with respect to partial melting. One of the main features in this diagram is the occurrence of a broad high variance field ($v = 4$) at high pressure (> 0.6 GPa) and high temperature (*c.* > 600 °C), in which the assemblage Grt–Pl–Kfs–Als–Qtz is stable. Because garnet is the only ferromagnesian phase in this assemblage, the predicted garnet composition is almost constant ($X_{Mg} = 0.46$–0.47) over the entire stability field. This quadrivariant assemblage corresponds to the peak assemblage observed in the felsic granulite of this study and is consistent with independent *P–T* determinations inferred from spatially associated metamorphosed mafic dykes (see ellipse and caption in Fig. 6a) (Williams *et al.*, 1995). In this range of *P–T* conditions, predicted compositions and modes of garnet and plagioclase from the pseudosection agree well with the sample (Table 4). The anhydrous *P–T* section predicts that decompression from peak conditions (*c.* 1.1 GPa), whether near isothermal or with decreasing temperature, has almost no effect on the assemblage until 0.6 GPa at 700 °C where orthopyroxene would be produced.

To model the hydrous retrograde assemblage, a *P–T* section was constructed using the S32D bulk composition and including 1.0 wt% H_2O (Fig. 6b). This water content was chosen to approach the H_2O-saturated conditions for the assemblage Bt–Crd–Pl–Grt–Sil–Qtz at *c.* 0.5 GPa (see Discussion below).

The addition of water leads to a considerably more complex *P–T* section (Fig. 6b). Some basic features are overlaid on the diagram in Fig. 6(c) including mode = 0 boundaries for selected phases, the solidus, and the H_2O-saturated fields. In strict terms, the boundaries between fields of different variance in these sections mark the locus of points at which the mode of one phase goes to zero. However, it is useful to correlate these boundaries and adjacent fields with reactions that may be more familiar in petrogenetic grids. For example, the narrow trivariant field for Bt–Crd–Pl–Grt–Sil–Qtz–H_2O, associated with the first appearance of Crd ('Crd-in' in Fig. 6c), is comparable with the KFMASH (degenerate) divariant reaction (3). The specified amount of H_2O in the bulk composition (1.0 wt%) is not sufficient to cause H_2O-saturation over the entire diagram. Only assemblages at high temperature (> *c.* 640 °C) and high pressure (*c.* > 0.6 GPa) or very low pressure are H_2O-saturated. The position of the H_2O-saturation line is controlled by the appearance of chlorite on the low temperature side of the diagram, by reactions involving production of cordierite at lower pressure, and by the loss of biotite at very high temperature and very low pressure. Consequently, the solidus itself is not saturated in H_2O for all pressures, resulting in an irregular geometry, but which is consistent with the theoretical analysis of Vielzeuf & Schmidt (2001) regarding phase relationships during melting as a function of bulk H_2O content.

The hydrous retrograde assemblage Bt–Crd–Pl–Grt–Sil–Qtz observed in sample S32D is predicted to be in equilibrium in subsolidus conditions in a narrow *P–T* field occurring between *c.* 0.6–0.4 GPa and 730–570 °C (triangular field highlighted in Fig. 6c). These conditions are consistent with the lack of evidence for melting and are within the estimated error of *P–T* conditions calculated from the retrograde phase equilibria (Fig. 6c). Figure 6(d–e) shows selected compositional and modal isopleths for garnet and cordierite in the region of the retrograde assemblage stability field, and predicted *v.* observed compositions are listed in Table 4. The observations that the predicted X_{Mg} in garnet is slightly higher than that observed in this sample and that the calculated temperatures (575–520 °C) overlap the predicted stability field only at the low-*T* end support our suggestion that the calculated temperatures are minima. Therefore, a temperature of *c.* 650 °C is adopted, corresponding to the centre of the retrograde assemblage stability field in Fig. 6(b), for subsequent analysis.

P–M_{H_2O} phase diagram section

From thermobarometric data and observations discussed above, the retrograde evolution of the felsic granulite is characterized by decompression from 1.1–

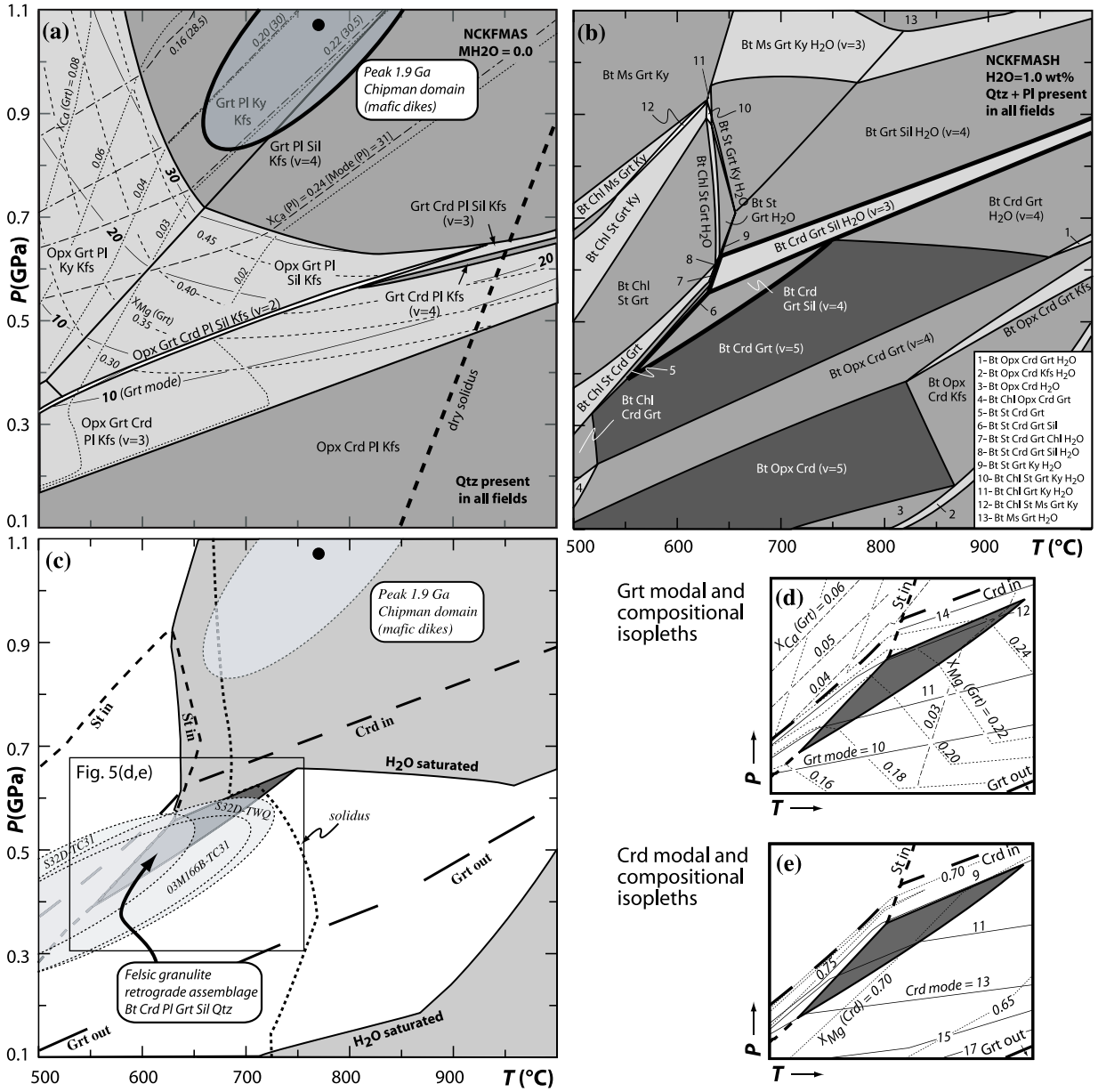

Fig. 6. *P–T* pseudosections. Quartz and plagioclase are present in all fields. (a) Anhydrous NCKFMAS section for anhydrous felsic granulite 02M129E composition. Water content = 0.0 wt%. Heavy dashed line indicates dry solidus. Various light dashed lines are compositional isopleths. Light solid lines are garnet modal isopleths (vol.%) – note that essentially all of the high *P–T* $v = 4$ field for the peak assemblage has garnet mode between 30 and 32.5 vol.%. The *P–T* ellipse (2-σ), plotted at 1.07 ± 0.19 GPa, 773 ± 92 °C (corr. = 0.79), is the weighted mean of five Chipman mafic dykes (including those reported by Williams *et al.*, 1995) individually calculated using Thermocalc 3.1. Two dykes have assemblage Grt–Hbl–Pl–Qtz, three dykes have Grt–Cpx–Hbl–Pl–Qtz. All iron is assumed to be ferrous. Williams *et al.* (1995) reported *P–T* estimates of *c.* 1.0 GPa, 750–850 °C for several dyke samples, but suggested that peak temperatures probably reached at least 800 °C. A minimum of 800 °C is consistent with the peak sillimanite-bearing felsic granulite assemblage shown here, noting that the dyke *P–T* ellipse overlaps the sillimanite field at the high-*T* edge. (b) NCKFMASH section for hydrous retrograde felsic granulite S32D composition. Water content = 1.0 wt%. Heavy lines mark fields specifically mentioned in text. (c) Same section as in (b) highlighting the phase assemblage boundaries that correspond to staurolite-in, cordierite-in and garnet-out. Calculated melt solidus is also shown. Ellipses are 2-σ uncertainty for peak (same as in (a)) and retrograde *P–T* conditions calculated with TWQ and Thermocalc 3.1 (TC31) software. (d) Compositional and modal (vol.%) isopleths for garnet in the region around the retrograde assemblage stability field. (e) Cordierite compositional and modal isopleths.

1.0 to 0.5–0.4 GPa and cooling from *c.* 800 to 650 °C under subsolidus conditions. The *P–T* sections presented in Fig. 6 represent essentially end-members with respect to H_2O content and do not provide an accurate representation of the dependence of assemblages on H_2O content during the entire evolution. *P–*M_{H_2O} and

Table 4. Comparison of pseudosection predicted *v.* observed phase compositions.

	Anhydrous felsic granulite				Hydrous retrograde felsic granulite							
	P–T (H_2O = 0.0 wt%) at 1.07 GPa, 800 °C				*P–T* (H_2O = 1.0 wt%) at 0.5 GPa, 650 °C							
	Garnet		Plagioclase		Garnet		Plagioclase		Biotite		Cordierite	
Molar proportions	Predicted	Observed (02M129E) rim	Predicted	Observed (02M129E)	Predicted	Observed (S32D)	Predicted	Observed (S32D) rim	Predicted	Observed (S32D)	Predicted	Observed (S32D)
Si	3.00	3.03	2.79	2.78	3.00	2.96	2.72	2.64	2.65	2.63	5.00	4.95
Al	2.00	1.95	1.20	1.21	2.00	2.03	1.28	1.36	1.70	1.66	4.00	4.05
Fe	1.47	1.51	0.00	0.00	2.29	2.36	0.00	0.01	1.15	1.25	0.58	0.53
Mg	1.42	1.38	0.00	0.00	0.60	0.46	–	–	1.50	1.44	1.42	1.47
Ca	0.11	0.11	0.21	0.24	0.12	0.10	0.28	0.32	–	–	–	–
Na	–	–	0.80	0.75	–	–	0.72	0.70	–	0.03	–	0.03
K	–	–	0.00	0.02	–	–	0.00	0.01	1.00	0.80	–	–
Molar ratios												
X_{Mg}	0.47	0.46	–	–	0.20	0.16	–	–	0.57	0.54	0.71	0.74
$X_{Ca(Gr)}$	0.037	0.037	–	–	0.040	0.033	–	–	–	–	–	–
$X_{Ca(An)}$	–	–	0.21	0.24	–	–	0.28	0.31	–	–	–	–
Mode	32	29	30	30	11	9	31	30	19	24	11	8

See caption to Fig. 6 for discussion of choice of temperature of 800 °C for anhydrous granulite.

T–M_{H_2O} diagrams offer the opportunity to model an open system behaviour with respect to water under subsolidus conditions (e.g. Guiraud *et al.*, 2001). Following Guiraud *et al.* (2001), M_{H_2O} is used to represent water content in order to avoid confusion with the commonly used variable X_{H_2O} for fluid composition.

A P–M_{H_2O} pseudosection calculated at 650 °C and for the retrograde granulite S32D bulk composition is presented in Fig. 7(a). All assemblages are subsolidus at this temperature. In this diagram, decompression is constrained to be isothermal, but cooling is considered in the following discussion. The abscissa represents normalized water content, where a value of zero corresponds to anhydrous conditions and 1.0 is equivalent to 1.5 wt% H_2O, a condition for which all assemblages are H_2O-saturated. The left side of the diagram shows the stability field of the anhydrous assemblages ($M_{H_2O} = 0$). The H_2O-saturation line, which delimits the minimum water content to stabilize a free fluid phase, and the value of M_{H_2O} used to construct Fig. 6(b) are shown as a thick black line and arrow on the x-axis, respectively.

The evolution of the felsic granulite begins at point **A** (*c.* 1.1–1.0 GPa, anhydrous) in Fig. 7(a) and ends at point **D** (0.5–0.4 GPa, hydrated). Modal changes predicted along the P–M_{H_2O} path at 650 °C are presented in Fig. 7(b–c). Textural observations and independent constraints on absolute timing (see below) suggest that the P–T–M_{H_2O} evolution can be divided into three distinct stages. (1) An initial anhydrous decompression stage occurred from 1.1–1.0 to 0.8–0.7 GPa (point **B**), which could have been accompanied by cooling from the peak metamorphic temperature. The subsolidus character of the decompression textures precludes the possibility that hydration initially occurred near peak conditions. Any fluid influx involving H_2O-saturation above 0.7 GPa and *c.* 670 °C (minimum temperature of the fluid-present solidus) would result in partial melting, for which there is no evidence. Decompression to *c.* 0.7 GPa is further substantiated by the occurrence of sillimanite as the alumino-silicate phase that accompanied biotite upon hydration. During this stage, under near anhydrous conditions, the peak assemblage essentially remains stable as demonstrated in Fig. 6(a). Very limited garnet consumption along this path (Fig. 7b) produces a small amount of retrograde plagioclase (Fig. 7c), which may account for increased Ca content at the margins of matrix plagioclase in retrograde granulite S32D. If anhydrous decompression proceeded much below 0.7 GPa, orthopyroxene would have been expected. No evidence for orthopyroxene is observed. (2) A period of near isobaric hydration at *c.* 0.7 GPa resulted first in biotite growth at the expense of garnet and K-feldspar in the quadrivariant (NCKFMASH) field for Bt–Pl–Grt–Sil–Kfs–Qtz. This assemblage is similar to reaction (2) but with the addition of plagioclase as a product (Fig. 7c). If initial H_2O-saturation was achieved above *c.* 0.7 GPa, then small amounts of staurolite would be expected. No evidence for staurolite is observed. (3) At this pressure (*c.* 0.7 GPa), cordierite is not produced until near H_2O-saturated conditions at point **C**. Continued decompression proceeded to 0.5–0.4 GPa under near H_2O-saturated conditions with more cordierite production (point **D**) through reaction (3). A P–M_{H_2O} section calculated at 600 °C results in orthopyroxene and staurolite stability extending to higher pressures (*c.* 0.8 GPa for Opx) under dry and near H_2O-saturated conditions, respectively, but does not change significantly in the regions of interest nor does it change the interpreted evolution.

Stages 1–3 could have occurred continuously during a single decompression event. However, new *in situ* monazite geochronology presented below, along with consideration of existing geological and geochronological constraints, suggest that decompression (exhu-

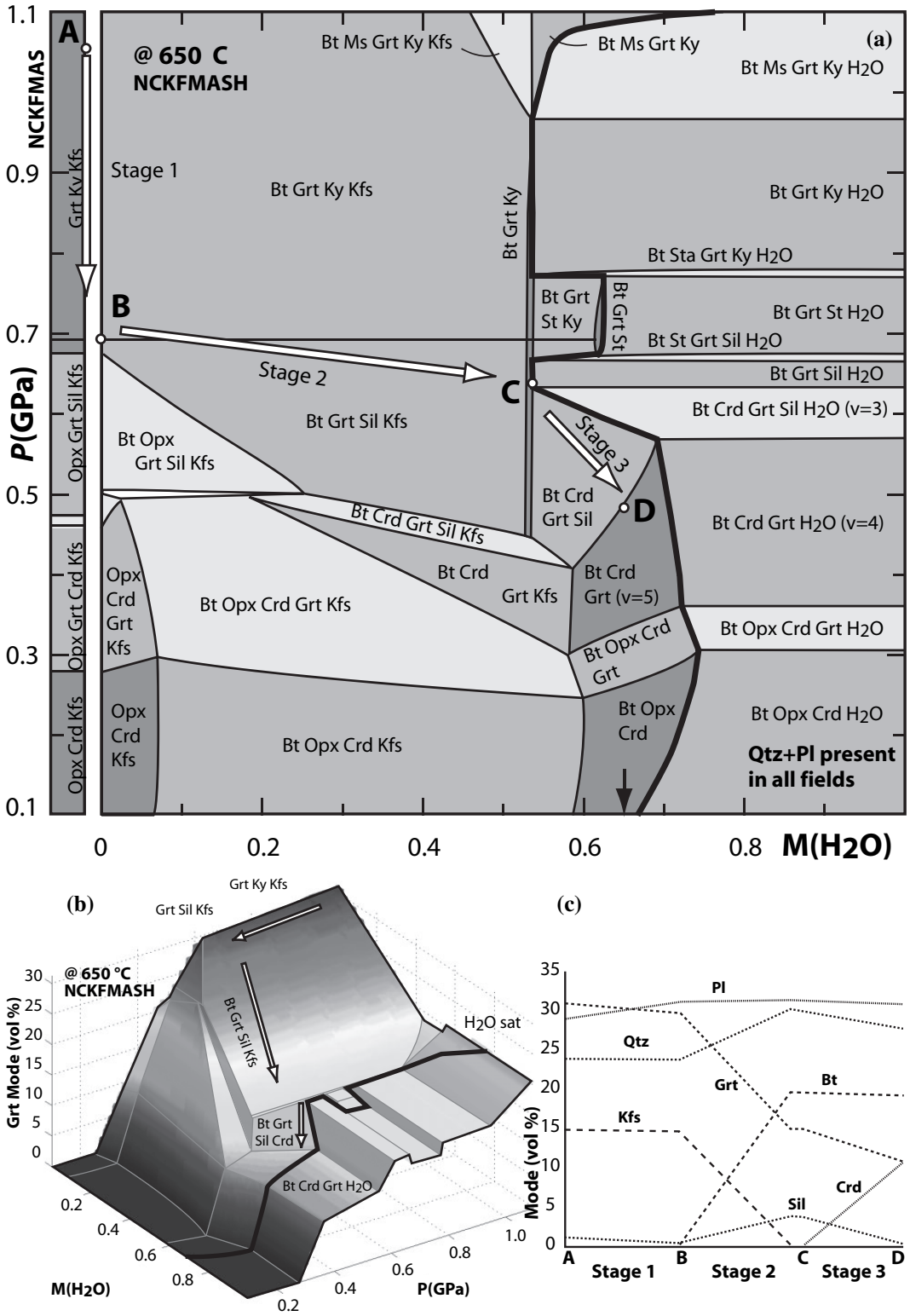

Fig. 7. (a) P–M_{H_2O} pseudosection for retrograde granulite S32D composition. Thick black line marks H_2O saturation. Black arrow along x-axis indicates water content corresponding to the P–T sections in Fig. 5(b,c). Quartz and plagioclase are present in all fields. (b) P–M_{H_2O}–Grt mode diagram. (c) Plot of modal changes for individual phases along the P–M_{H_2O} path A–B–C–D shown in (a).

mation) and retrograde evolution of the felsic granulite was discontinuous and occurred over a considerable period of time.

MONAZITE GEOCHRONOLOGY

Monazite is abundant in both anhydrous and hydrous retrograded felsic granulite and can be divided into at least five distinct populations on the basis of composition, textural setting and age. In contrast, xenotime is present only in the hydrous retrograded felsic granulite. Data from the three samples described above are presented. Monazite distribution and characteristics are similar in all three samples, but particular attention is paid to sample S32D, in which all five populations were first identified.

Analytical methods and procedure

The methods used for evaluating and analysing monazite follow those of Williams & Jercinovic (2002) and Jercinovic & Williams (2005). All analyses were conducted at the University of Massachusetts-Amherst electron microprobe facility. X-ray maps and wavelength-dispersive spectrometric analyses for major elements in monazite were made using a Cameca SX-50 microprobe. The occurrence, distribution and textural setting of monazite were first evaluated using full thin section X-ray composition maps of Ce for identification of monazite and a reference major element (Mg) to establish the overall texture (Fig. 4a). High-resolution (beam scanning) X-ray maps of Y, Th, U and Pb and/or Ca were generated for each grain.

Quantitative major element analyses were acquired for representative compositional domains and used both to further characterize textural or compositional populations and for entry into the trace element analytical routine for calculation of mass absorption factors. Analytical conditions are given in Table 5. Quantitative trace element analyses were performed either with the 4-spectrometer Cameca SX-50 or with the 5-spectrometer Cameca SX-100 *Ultrachron*, which is specifically designed for maximum precision in trace element analysis (the machine used is designated in Table 5). Prior to trace element analysis, background intensities for Y Lα, Th Mα, U Mβ and Pb Mα (also K Kβ for SX-100 analyses – see below) were evaluated for each compositional domain based on regression of spectrometer step scans.

Corrections were made for Th Mζ and Y Lγ interferences on Pb Mα and for Th Mγ interference on U Mβ. For SX-50 trace element data, interference corrections were performed offline and post-ZAF correction using a correction factor applied to the element concentrations (Pyle *et al.*, 2002). For SX-100 data, interference corrections were made prior to ZAF-corrections via application of overlap intensities calibrated from interference standards (e.g. Jercinovic & Williams, 2005). In addition, monazite trace element analysis within *c.* 15 μm of the edge of the grain may induce fluorescence of K X-rays from adjacent K-bearing phases (e.g. K-feldspar, biotite), and therefore may be affected by K Kα interference on U Mβ (Jercinovic & Williams, 2005). For this reason, in all monazite domains where this effect was expected, analysis of K Kβ was performed with the SX-100 in order to correct the K Kα–U Mβ overlapping interference.

The method of calculating dates and errors follows Williams *et al.* (2006). For each homogeneous compositional domain, at least three and typically 5–20 trace element analyses were obtained. Weighted mean compositions of Th, U and Pb were calculated based on the analytical uncertainties from counting statistics for each analysis. A single date for that domain was then calculated from the weighted mean compositions and the age equation of Montel *et al.* (1996). The 2-σ error reported here (Table 5), calculated by propagating the analytical uncertainty on trace element compositions through the age equation, represents short-term analytical precision as noted by Williams *et al.* (2006). Uncertainty associated with the background regression may increase the total error by 50–100%. Data for multiple age domains are displayed graphically in the form of normal distribution curves. Weighted means of dates from multiple domains were calculated using the Isoplot/Ex v. 3 program of Ludwig (2003) with 95% confidence errors. Data from one of two consistency standards for each analytical session (except 2002 data) are also reported in Table 5. Wards Elk Mtn monazite [*c.* 1395 Ma by ID-TIMS (J. Baldwin & S. Bowring, personal communication, 2005)] has a 3-month (15 sessions) average of 1390 ± 22 Ma (2 SD). Standard GSC 8153 [*c.* 500 Ma by ID-TIMS and SHRIMP (W. Davis & N. Rayner, personal communication, 2005)] has a 2.5-month (14 sessions) average of 498 ± 8 Ma (Williams *et al.*, 2006).

Occurrence, distribution and compositional zoning

Monazite grains range in size (mean diameter) from 15 to 200 μm, and occur in the matrix and within domains of partially replaced garnet in the hydrated samples (S32D and 03M166B) (Figs 4a & 9a). Monazite inclusions in garnet are common in the anhydrous felsic granulite (02M129E) where the porphyroblasts are still intact, but are rarely preserved in the hydrous retrograde felsic granulite. Zoning of monazite is commonly evident in all elemental X-ray maps. However, Y shows the most consistent and distinctive zonation with concentration variation of more than an order of magnitude (Fig. 8). Using core-rim geometric relationships and Y concentration, five populations of monazite were distinguished. Individual grains display a variety of combinations of the populations, but the relative sequence of interpreted growth is consistent. In the following section, absolute values for Y concentrations quoted in the

Table 5. Trace element compositions and microprobe age data.

					Trace element conc. (ppm)										
EMP	Date analysed	Grain	Setting	Domain	Y	1σ	Th	1σ	Pb	1σ	U	1σ	N	Date (Ma)	2σ (Ma)
Anhydrous felsic granulite 02M129E (UTM N:6587259, UTM E:477047)															
SX-50	16/05/2004	m9	ig	pop 1	21 133	14	49 668	65	11 327	19	10 856	18	11	2558	13
SX-50	16/05/2004	m3	ig	pop 1	16 522	12	40 963	44	11 131	17	12 471	17	13	2570	11
SX-50	16/05/2004	m7	m	pop 2	2693	9	59 887	128	10 540	30	6973	26	4	2533	24
SX-50	16/05/2004	m8	m	pop 3	394	4	3138	12	1159	10	1984	11	10	2262	50
SX-100	25/01/2005	m6	m	pop 3	552	5	1039	7	745	5	1648	10	6	2160	43
SX-50	02/02/2003	m1	m	pop 3	5492	7	13 551	24	3767	15	6077	17	8	2176	23
SX-100	25/1/2005	m6	m	pop 4	615	4	3807	12	1010	4	2031	8	9	1909	24
Hydrous retrograded felsic granulite S32D (UTM N:6606210, UTM E:495256)															
SX-50	30/5/2004	1-m8	m	pop 1	13 263	15	31 370	76	6066	25	4851	24	4	2519	33
SX-50	03/11/2002	2-m2	m	Pop 1	12 915	11	36 149	47	6992	18	5394	18	7	2553	22
SX-50	30/05/2004	2-m4	m	pop 1	10 196	15	38 213	106	7614	32	6380	30	3	2521	32
SX-100	29/04/2005	2-m7	m	pop 1	22 125	64	35 178	166	11 066	5	14 300	32	13	2524	14
SX-50	09/06/2002	1-ml	m	pop 2	3730	4	40 233	35	8631	14	8268	14	17	2491	12
SX-100	29/04/2005	2-m7	m	pop 2	7433	25	41 394	212	9624	5	9556	24	11	2544	18
SX-50	30/05/2004	2-m1	m	pop 2	5357	10	41 569	99	9225	30	9240	29	4	2486	24
SX-50	09/06/2002	1-m1	m	pop 3	773	4	48 226	53	7925	17	5003	16	10	2462	16
SX-100	03/05/2005	1-m10	m	pop 3	291	6	56 476	345	7671	6	1904	9	8	2529	31
SX-100	03/05/2005	1-m10b	m	pop 3	1159	11	44 707	386	7422	8	4449	20	4	2510	37
SX-100	05/05/2005	2-m3	m	pop 3	666	7	27 895	171	4036	5	1747	10	8	2453	32
SX-50	30/05/2004	2-m5	m	pop 3	368	7	54 690	113	7075	24	1600	20	5	2455	29
SX-100	29/04/2005	2-m7	m	pop 3	232	6	98 603	591	12 222	7	908	5	8	2528	31
SX-100	01/05/2005	2-m14	m	pop 3	429	6	53 118	135	7884	6	3228	11	9	2523	17
SX-50	30/05/2004	2-m5	m	pop 3	622	6	22 564	48	3875	18	3461	19	6	2287	31
SX-100	30/05/2005	1-m8	m	pop 4	1418	9	34 285	210	4254	5	3840	13	8	1884	22
SX-50	30/05/2004	1-m7	m	pop 4	1283	4	30 097	36	4154	11	4420	12	16	1916	15
SX-100	03/05/2005	2-m3	m	pop 5	8519	33	14 497	89	1484	4	713	8	8	1863	33
SX-100	29/04/2005	2-m7	m	pop 5	9086	40	21 206	116	2053	5	777	10	6	1836	30
SX-100	03/05/2005	1-m8	m	pop 5	8448	53	16 668	167	1712	7	910	13	3	1839	50
SX-100	03/05/2005	2-m14	m	pop 5	9516	31	13 989	67	1751	4	880	7	11	1861	24
Hydrous retrograded felsic granulite 03M166B (UTM N:6623325, UTM E:506186)															
SX-100	29/05/2005	m28	ig	pop 0/1?	779	7	54 322	138	7745	6	2144	11	7	2593	19
SX-100	29/05/2005	m6	m	pop 1	10 424	35	52 704	134	8024	6	3700	12	7	2510	19
SX-100	29/05/2005	m7	m	pop 1	14 078	32	37 313	76	6296	5	4113	12	12	2482	15
SX-100	05/05/2005	m1	m	pop 4	2307	9	24 843	46	2629	4	1241	9	9	1916	15
SX-50	16/05/2004	m17	m	pop 4	1401	6	38 917	54	3835	15	1174	15	8	1903	23
SX-50	09/05/2004	m14	is	pop 4	356	5	32 682	51	3342	15	1166	15	8	1937	27
SX-100	29/05/2005	m26	m	pop 4	319	6	7526	22	844	4	554	10	7	1892	38
SX-100	05/05/2005	m1	m	pop 5	14 129	23	28 981	36	2779	3	902	5	19	1851	10
SX-50	08/05/2004	m17	m	pop 5	15 429	13	30 958	43	3144	13	1491	14	10	1855	23
SX-100	05/05/2005	m26	m	pop 5	5836	24	6250	20	686	5	497	13	4	1827	53
Consistency standard Ward's Elk Mtn – 3-month average of 1390 ± 22 Ma (2 SD) – dated at *c.* 1395 Ma by ID-TIMS															
SX-50	08/05/2004	–	–	–	5108	13	123 612	274	8687	34	3465	31	3	1392	18
SX-50	09/05/2004	–	–	–	4912	11	122 615	217	8678	29	3478	26	4	1400	15
SX-50	16/05/2004	–	–	–	5242	10	126 638	231	8905	26	3374	24	5	1399	14
SX-50	30/05/2004	–	–	–	5106	10	122 345	242	8669	27	3424	24	5	1403	15
Consistency standard GSC 8153 – 2.5-month average of 498 ± 8 Ma (2 SD) – dated at *c.* 500 Ma by ID-TIMS															
SX-100	25/01/2005	–	–	–	4217	8	65 610	219	1640	6	2528	10	5	494	7
SX-100	29/04/2005	–	–	–	4252	22	63 911	484	1591	5	2607	15	5	489	10
SX-100	01/05/2005	–	–	–	4278	16	64 172	157	1595	3	2591	9	10	489	4
SX-100	03/05/2005	–	–	–	4213	22	64 243	496	1620	5	2487	13	5	498	10
SX-100	05/05/2005	–	–	–	4310	17	64 220	155	1663	5	2514	16	5	511	6
SX-100	29/05/2005	–	–	–	4321	20	64 475	208	1625	5	2518	14	5	498	6

Analytical conditions: Major element analysis and trace element calibration (SX-50) −15 kV, 15 nA, 20 s peak, 10 s background, focused beam. Trace element calibration (SX-100) −15 kV, 20 nA, 20 s peak, 10 s background, focused beam. Trace element analysis (SX-50) −15 kV, 200 nA, 600 s peak. Trace element analysis (SX-100) −15 kV, 200 nA, 800 s each for Y, Th and Pb, 500 s for U, 300 for K. In Grain column, # preceding 'm' corresponds to one of two thin sections from same billet. In 'Setting' column, m = matrix, ig = inclusion in garnet, is = inclusion in sillimanite, Y Lα measured on TAP with SX-50 and on PET with SX-100. Th Mα measured on PET with SX-50 and on LPET with SX-100. Pb Mα measured on PET with SX-50, on two spectrometers with VLPET (very large) on SX-100, and corrected for Y and Th interferences. U Mβ measured on PET with SX-50 and on LPET with SX-100. Corrected for Th on SX-50 and both Th and K interferences on SX-100. Age error does not include uncertainties on background regression which may increase total error by 50–100%.

text and shown in Fig. 8 refer specifically to retrograde granulite S32D.

Population 1 generally contains the highest Y concentrations (10 000–22 000 ppm, Table 5) and occurs as distinct innermost cores (Fig. 10a,d,g,j) or as rare whole grains. In the anhydrous granulite 02M129E, population 1 monazite occurs primarily as inclusions in garnet (Fig. 11e,f). Population 2 (4000–8000 ppm Y) commonly occurs as a mantle domain surrounding population 1 monazite (Fig. 10a,j,e). Populations 3 and 4 are restricted to and dispersed throughout the matrix. They contain the lowest Y concentrations (< 1000 and 1300–1400 ppm, respectively) and occur either as mantles surrounding higher Y population 1 or 2 (Fig. 10a,d,g,j) or as the core domains in grains with population 5 rims (Fig. 11a–c). One apparent exception is a small homogeneous low Y monazite grain that occurs as a clean inclusion in garnet in the hydrous

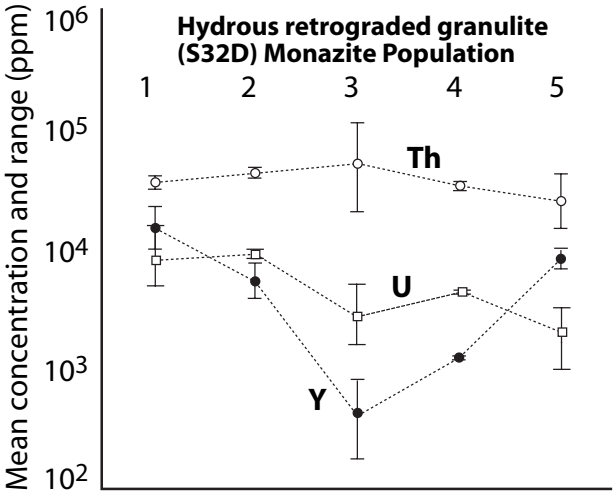

Fig. 8. Plot showing variation in Y, Th and U among five monazite populations in retrograde felsic granulite S32D.

retrograde granulite 03M166B (*c*. 800 ppm Y; m28 in Table 5). Population 5 occurs as discontinuous overgrowths that are present only in the retrograded granulite (Figs 10a,d,g,j & 11a–c, and is spatially associated with resorbed garnet porphyroblasts (Fig. 10b,e,h,k). Population 5 overgrowths are better developed near the outer margins of garnet porphyroblasts (Figs 9a & 11b,e,h,k) and they are commonly in contact with biotite. This population has distinctly higher Y concentrations (8000–10 000 ppm) than adjacent domains (i.e. populations 3 or 4). These observations suggest a genetic link between population 5 monazite and garnet-breakdown. In addition, small (5–10 μm) apatite grains are closely associated with the monazite overgrowths (Fig. 10a,d,g,j). Although we cannot rule out the possibility that apatite formed first and was then consumed during growth of population 5 monazite, coeval crystallization of both phases is suggested based on the generally mutually exclusive occurrence of apatite or monazite overgrowths in contact with older monazite cores (i.e. clear overgrowths of either monazite or apatite on the other are absent). Xenotime is present only in the retrograded granulite and occurs as small grains (typically 5 μm or less) only within the 'interior' of relict garnet porphyroblasts where cordierite is the dominant replacement phase (Fig. 9b,c).

Interpretation of textural relationships and zoning patterns

Recent studies have shown that the petrogenesis of monazite and xenotime is strongly influenced by major silicate net-transfer reactions involving garnet growth or consumption (e.g. Pan, 1997; Bea & Montero, 1999; Pyle & Spear, 1999, 2000, 2003; Foster *et al*., 2000, 2004; Spear & Pyle, 2002; Foster & Parrish, 2003; Gibson *et al*., 2004; Kohn & Malloy, 2004; Berman *et al*., 2005; McFarlane *et al*., 2005). This is because garnet is commonly one of the only major silicate phases that incorporate significant trace quantities of Y and heavy rare earth elements (HREEs). Consequently, reactions involving garnet can have a profound influence on the Y and REE budgets in the rock

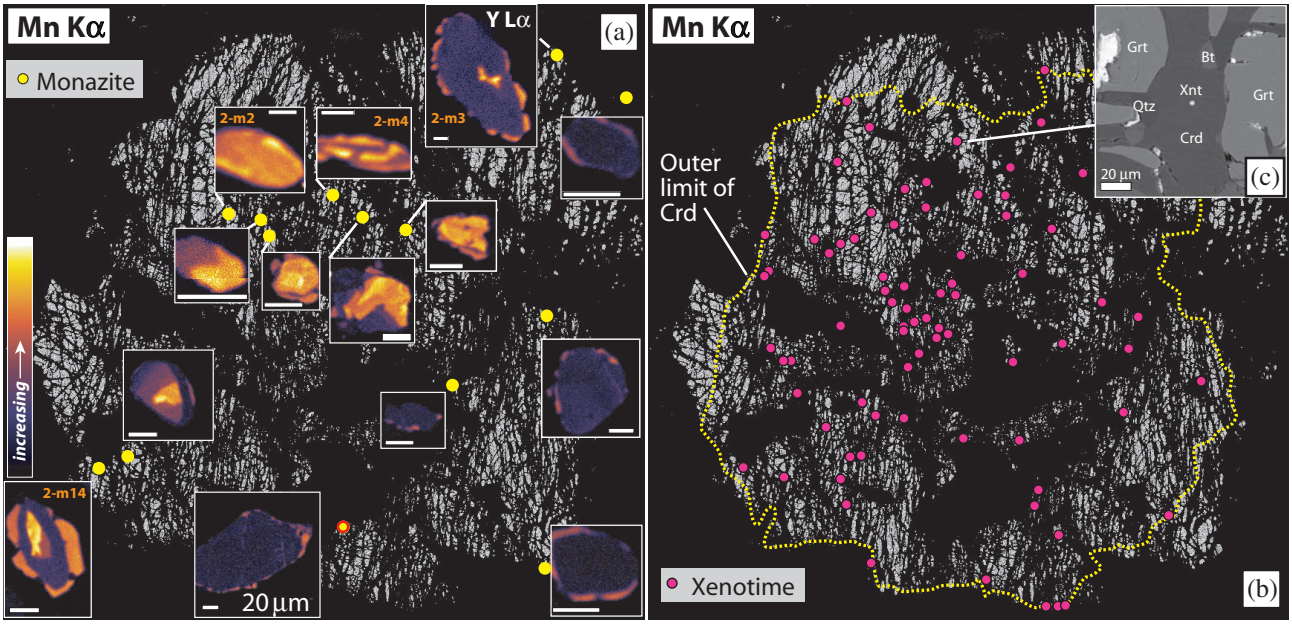

Fig. 9. (a) Monazite distribution within and around the margins of retrograde granulite S32D garnet. Y X-ray maps of individual grains have proportionately scaled colour tables. White scale bar is 20 μm in all X-ray maps. Background is greyscale Mn X-ray map. (b) Locations of xenotime within S32D garnet. Note the restriction of xenotime to within the Crd-reaction zone. (c) Backscatter electron image showing textural setting of xenotime included within cordierite.

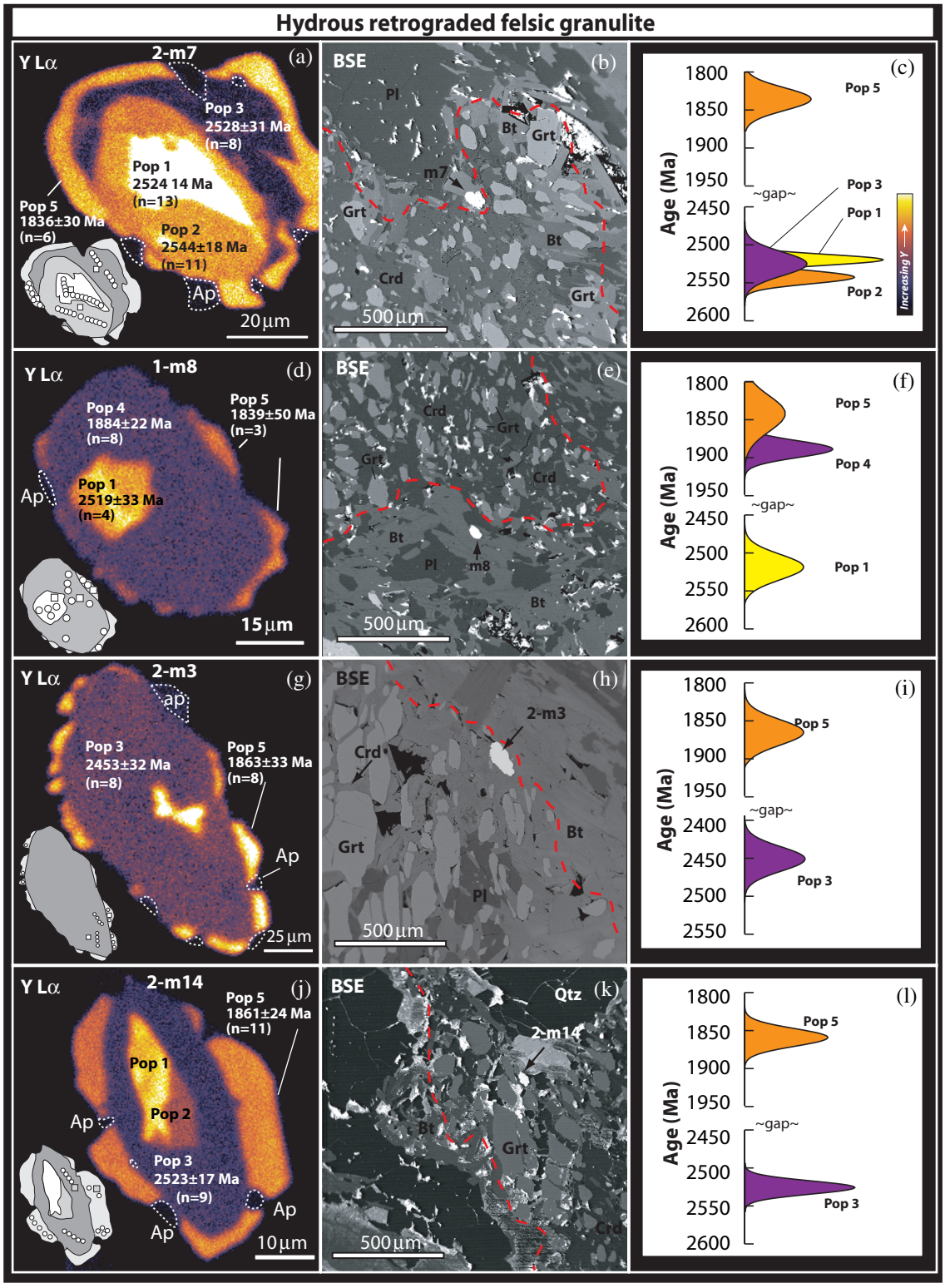

Fig. 10. Monazite from hydrous retrograde felsic granulite S32D: 2-m7 (a–c), 1-m8 (d–f), 2-m3 (g–i), 2-m14 (j–l). (a, d, g, j) Y Lα X-ray maps. Distribution of small apatite grains (Ap) shown with white dashed line. Inset shows line-drawing of monazite grain delineating compositional domains and showing the location of individual spot analyses (circles) and background wavelength scan spots (squares). (b, e, h, k) Backscatter images showing the textural setting of each monazite. Note the proximity of each monazite grain to the outer margin of relict garnet porphyroblasts (red dashed line). (c, f, i, l) Normal distribution curves summarizing EMP dates for each grain. Each curve represents the date and error for a single compositional domain.

and, in turn, can impart a major influence on the petrogenesis of accessory phases that incorporate those elements. In this study, using textural observations and the distinct variations in Y concentrations in monazite, we suggest some first-order interpretations that relate monazite, xenotime and garnet growth and that can be tested for consistency by directly dating the accessory phases.

The presence as inclusions in garnet and the highest Y content suggest that population 1 monazite grew early in the metamorphic history, either prior to or during garnet growth and before significant depletion of the effective bulk Y budget. Some grains that are included in garnet also display overgrowths of population 2 monazite (Fig. 11e) suggesting that garnet growth continued during this phase of monazite production. However, the sharp compositional transition between populations 1 and 2 monazite, and textures consistent with a period of intermediate monazite resorption (Figs 10a & 11e), may further suggest that garnet growth was discontinuous. In contrast, monazite from populations 3 and 4, which are generally restricted to matrix settings and fractures within garnet, have the lowest Y concentrations suggesting that they grew in the presence of modally abundant, but relatively inert garnet. There is no evidence for the presence of xenotime during the growth of monazite populations 1–4.

The most compelling textural relationships are those related to the high Y monazite overgrowths (population 5), as well as spatially associated apatite and xenotime. The pervasive development of these phases in the vicinity of and inside the relict garnet porphyroblasts, and relatively high concentrations of Y and HREEs in the monazite overgrowths, indicate that accessory phase growth was related to garnet-breakdown. The P–M_{H_2O} section suggests that garnet-breakdown first involved biotite production through reaction (2) followed by cordierite via reaction (3). The predominant distribution of high-Y monazite (population 5) in the biotite-rich margins of garnet and the restriction of xenotime to the cordierite-rich interior of garnet suggest a more direct link to the net-transfer reactions (2) and (3), respectively.

Geochronology results

Results are listed in Table 5 and summarized in Fig. 12. Seven domains from population 1 yield dates between 2570 ± 11 and 2482 ± 15 Ma, including two

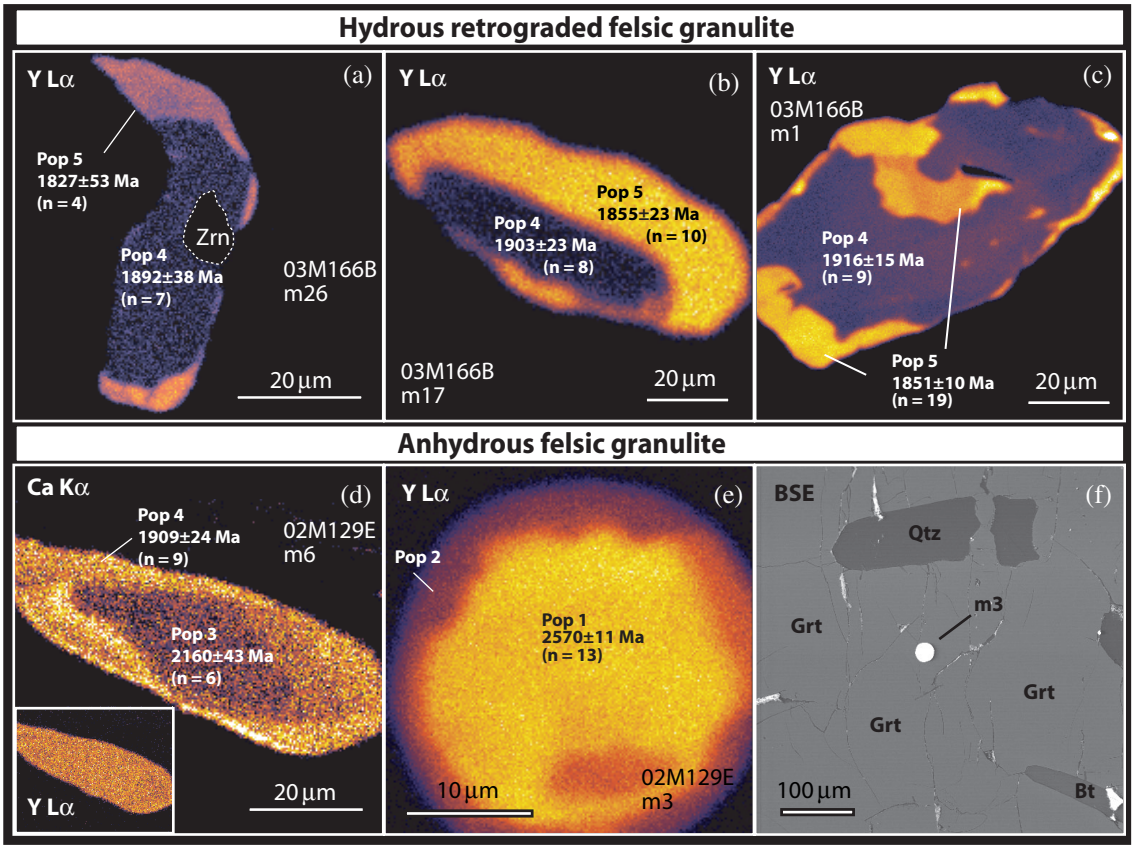

Fig. 11. Monazite from hydrous retrograde felsic granulite 03M166B and anhydrous felsic granulite 02M129E. (a–c) Y Lα X-ray maps of 03M166B m26, m17 and m1, respectively. (d) Ca X-ray map of 02M129E-m6. Inset is Y Lα X-ray map. (e) Y Lα X-ray map of 02M129E-m3 (inclusion in garnet). (f) BSE image of textural setting of 02M129E-m3.

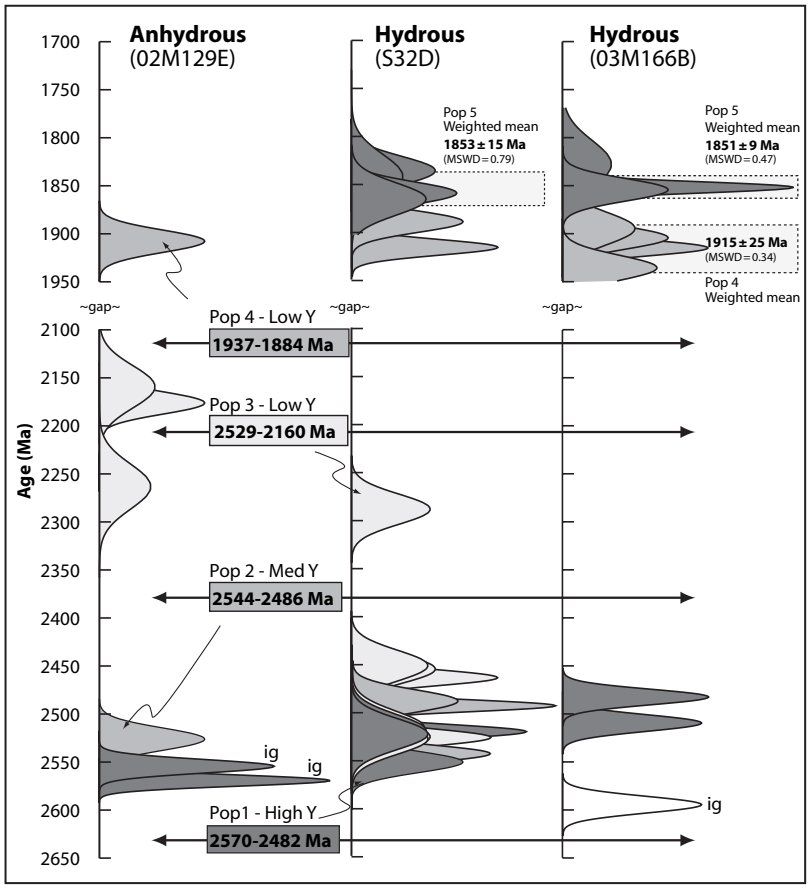

Fig. 12. Summary of EMP monazite geochronology for three samples. Each normal distribution curve represents the date and error for an individual compositional domain. The dashed rectangles shown for populations 4 and 5 monazite bracket the 95% confidence intervals for the weighted mean dates. ig = inclusions in garnet.

inclusions in garnet from 02M129E (Fig. 11f). Population 2 dates are indistinguishable from population 1 and range between 2544 ± 18 and 2486 ± 24 Ma. Population 3 domains yield a wide spectrum of dates between 2529 ± 31 and 2160 ± 43 Ma. Populations 4 dates range from 1937 ± 27 to 1884 ± 22 Ma with a weighted mean of four domains in sample 03M166B of 1915 ± 23 Ma (MSWD = 1.7). Population 5 dates range from 1863 ± 33 to 1827 ± 53 Ma with weighted mean dates from samples S32D and 03M166B of 1853 ± 15 Ma ($n = 4$, MSWD = 0.79) and 1851 ± 9 Ma ($n = 3$, MSWD = 0.47). Surprisingly, the monazite grain with the oldest date of 2593 ± 19 Ma is the single low Y inclusion in garnet from retrograde granulite 03M166B.

These data indicate several monazite growth episodes reflecting a long (> 600 Myr) tectonometamorphic history for the region. The age of population 1–2, which are the populations most closely associated with garnet growth, corresponds to the first of two major tectonometamorphic events that affected the high-*P* region. Hanmer *et al*. (1994) and Hanmer (1997) proposed high-*P* metamorphism in this area at *c*. 2.6 Ga based on the protolith ages of meta-granitoids. Based on more recent and higher resolution ID-TIMS data from metamorphic zircon, early high-*P* metamorphism is more tightly constrained to 2.55–2.52 Ga (Flowers, 2005; see also Baldwin *et al*., 2003, 2004). A 2.55–2.50 Ga period of medium-*P* regional metamorphism has also been recently recognized further north in the Rae and Hearne domains (Berman *et al*., 2000, 2002; Stern & Berman, 2000).

The *c*. 1.9 Ga monazite of population 4 correlates with the second period of major high-*P* event(s) in the region. These involved a second granulite facies overprint in mafic granulite and partial melting of mafic dykes at 1896 ± 0.3 Ma in the Chipman subdomain (Flowers *et al*., in press) and also involved local very high-*P* eclogite facies metamorphism in the southern subdomain at 1904 ± 0.9 Ma (Baldwin *et al*., 2003, 2004).

The *c*. 1850 Ma age of high Y population 5 monazite records the timing of major retrograde metamorphism via reaction (2) and associated deformation in the Legs Lake shear zone. Xenotime crystallization is interpreted to record a continuation of garnet-breakdown via reaction (3). Some studies have suggested that the upper thermal stability of xenotime commonly correlates inversely with garnet growth and increasing temperature through the range of 500–650 °C (Bea & Montero, 1999; Pyle & Spear, 1999, 2003) whereas other studies suggest that xenotime may be stable

under granulite facies conditions (e.g. Möller *et al.*, 2003; McFarlane *et al.*, 2005). Although factors other than temperature were certainly involved, the presence of xenotime in the granulite is clearly related to retrograde metamorphism and may also reflect the associated temperature decrease.

Exceptions that do not easily fit the above patterns include the one low Y monazite inclusion in garnet (03M166B-m28) whose date is older than any of the high Y population 1 monazite and the widely varied 2.5–2.1 Ga dates of population 3. Although the low Y content of 03M166B-m28 is similar to populations 3 and 4, the age of the grain precludes any relation to those populations. If the grain represents an earlier phase of growth prior to population 1 growth or if it is simply an old outlier of population 1 (note Th content is similar to population 1 – Table 5), then local disequilibrium at a scale smaller than the thin section must explain the dramatically different Y content. Similarly, the significance of 2.5–2.1 Ga population 3 monazite is uncertain. However, the homogeneous composition of these domains and the high spatial resolution of the electron beam make mixtures of older and younger monazite unlikely. Therefore, although these grains are similar in composition and in textural setting, they clearly do not represent a single age population and therefore cannot represent a singular geological event. Baldwin *et al.* (in press) presented a similar range of monazite dates (between 2.5 & 2.0 Ga) in an ID-TIMS and EMP study of anhydrous felsic granulite in the southern subdomain. They suggested an explanation involving fluid-mediated dissolution and reprecipitation. Although population 3 monazite dates do not correspond to tectonometamorphic events that are known to have significantly affected this region locally, it is possible that monazite growth or reprecipitation during this interval reflects minor deep-crustal fluid flow or thermal perturbations related to more distal events. For example, mafic dykes and sill complexes intruded much of the western Churchill province at *c.* 2.45 and 2.11 Ga (Heaman, 1994; Aspler & Chiarenzelli, 1998) and major tectonometamorphism has recently been recognized in much of the western Rae domain at *c.* 2.35 Ga (e.g. Berman *et al.*, 2005). More detailed analyses are required and are ongoing in order to better understand these complexities.

DISCUSSION

Metamorphic evolution of felsic granulite and relationships to monazite/xenotime growth

As suggested by Baldwin *et al.* (in press) for felsic granulite in the southern subdomain, we interpret the anhydrous assemblage (Grt + Sil + Kfs + Pl + Qtz) in the felsic granulite in the Chipman subdomain to have initially formed during late Archean (2.55–2.50 Ga) granulite facies metamorphism (Fig. 13). This is supported both by the textural setting of populations 1 and 2 monazite (i.e. included in garnet) and their high Y content, which suggests growth either prior to or coeval with garnet. It is also noted that the range of Y concentrations in monazite populations 1 and 2 paired with Y in garnet core and near rim, respectively, yield monazite/garnet coefficients between 30 and 100, similar to the equilibrium distribution coefficient of 46 determined by Hermann & Rubatto (2003) for similar granulite facies rocks. Furthermore, the low Y content in monazite from population 3 suggests that garnet was already present by the time the oldest population 3 monazite grew at *c.* 2.5 Ga. Metamorphic conditions for the 2.55 Ga event are not well-constrained from the felsic granulite, but mafic granulite from the Chipman subdomain that is interpreted to have formed at 2.55 Ga (Flowers, 2005) record conditions of 1.3 GPa, 850 °C (K. H. Mahan, unpublished data). Similarly, low Y content in 1.9 Ga monazite suggests that garnet was still stable during the second granulite facies event. Although we suggest that most garnet grew at *c.* 2.55 Ga, there remains the possibility that the high-Ca margins of garnet grew at 1.9 Ga, a possibility also implied by the work of Baldwin *et al.* (in press) for felsic granulite in the southern subdomain. Preliminary observations from other felsic granulite near this study in the Chipman subdomain indicate that numerous low Y monazite grains are included in high Ca marginal garnet. These inclusions, which have not yet been dated, may correlate with either population 3 or 4 of this study, and if the latter, then it will require some 1.9 Ga growth of garnet. More work is needed in order to understand whether the increased Ca in garnet rims reflects changes in P–T conditions (perhaps decreased T or increased P – see X_{Ca} (Grt) isopleths in Fig. 6a) or in effective bulk composition.

Regardless of the timing of growth of the garnet rims, the grossular content of marginal garnet is consistent with predicted equilibrium (Fig. 6a) at the P–T conditions constrained for 1.9 Ga metamorphism in the Chipman subdomain (i.e. 1.0–1.1 GPa, *c.* 800 °C from mafic dykes; Williams *et al.*, 1995; Mahan & Williams, 2005; Flowers *et al.*, in press). Consequently, we consider these conditions to correspond to the starting point for the stage 1 anhydrous decompression history of the hangingwall of the Legs Lake shear zone (Figs 13 & 14). A period of relatively high-T decompression to 0.8–0.7 GPa and 700–750 °C is also suggested by retrograde assemblages in mafic lithologies from the region. These include late Opx–Pl symplectite from mafic granulite in the southern subdomain (Kopf, 1999) and late Hbl–Pl symplectite from mafic granulite near the sample 02M129E locality (K. H. Mahan, unpublished data). This stage of decompression is interpreted to have occurred immediately following 1.9 Ga peak metamorphism because of the relatively high temperature of equilibration at this intermediate pressure.

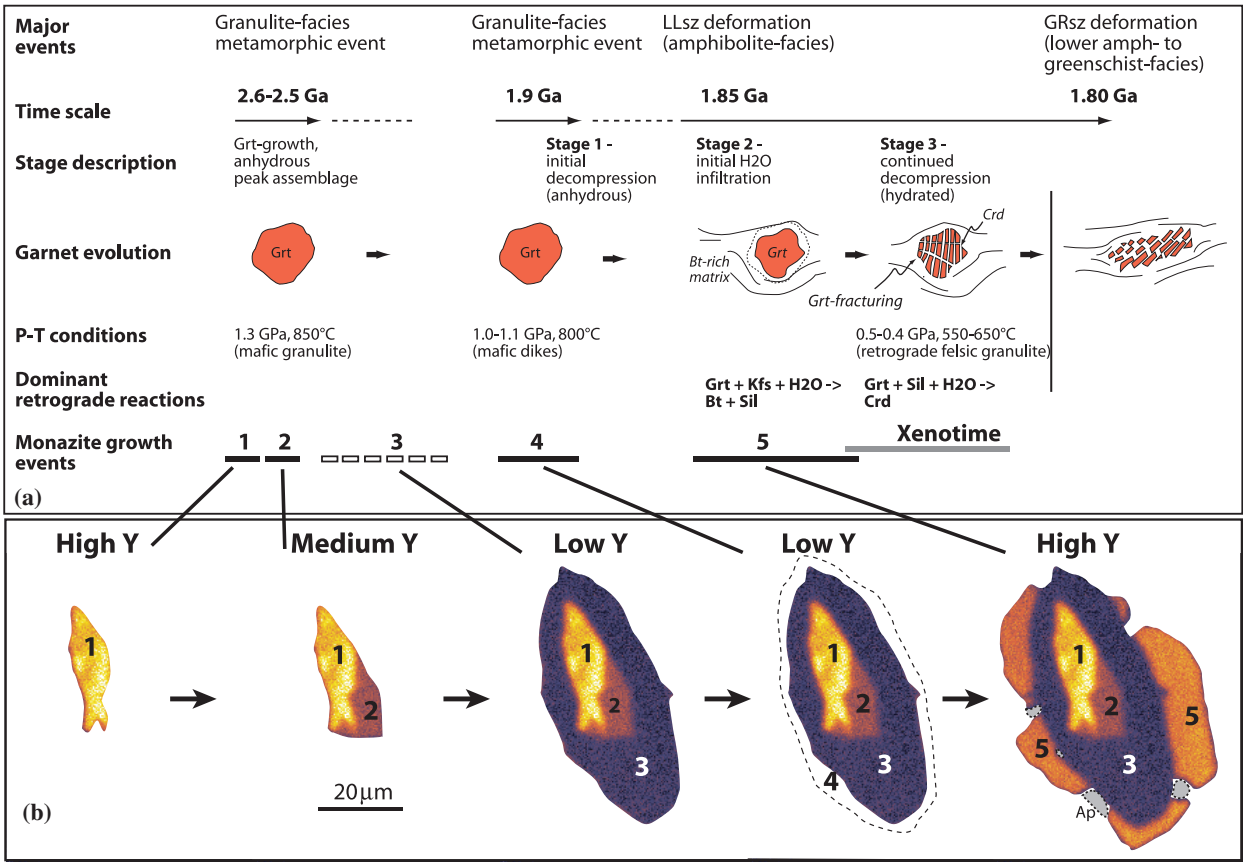

Fig. 13. (a) Summary model for evolution of felsic granulites in retrograde shear zones. (b) Illustration of corresponding monazite and xenotime growth. The growth of population 4 is schematically illustrated with dashed line. Possible intermediate periods of resorption are not shown. LLsz, Legs Lake shear zone; GRsz, Grease River shear zone.

The beginning of stage 2 infiltration of hydrous fluid at *c*. 0.8–0.7 GPa marked the onset of significant retrograde metamorphism of the felsic granulite in the Legs Lake shear zone. This hydration is manifested by the initial breakdown of garnet and K-feldspar to produce biotite via reaction (2). The observations that (1) biotite is a primary foliation-defining matrix phase and (2) the matrix fabric anastamoses around relict garnet porphyroblasts indicate that reaction (2) progressed synkinematically with deformation in the shear zone. Furthermore, it is suggested that the growth of high Y monazite population 5 and locally apatite was directly linked to this garnet-consuming reaction. Therefore, the age of this monazite (1.85 Ga) provides the best constraint on both deformation and the earliest stage of hydration in the shear zone.

Textural observations (Figs 2b & 4a,b) and phase diagram section analysis (Fig. 7a,c) indicate that significant biotite was generated in the matrix before cordierite production in the interior of fractured garnet porphyroblasts. Cordierite growth via reaction (3) is further correlated with the development of a dense network of fractures in the garnet. Fracturing must

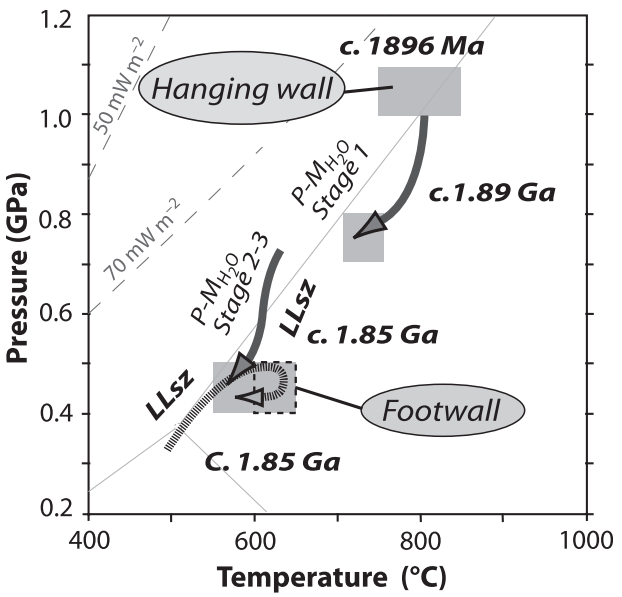

Fig. 14. Summary *P–T* path. Steady-state geotherms taken from Chapman & Furlong (1992).

have occurred during the hydration process and may reflect transient build up and release of fluid pressure in the shear zone. Continued decompression under hydrated conditions during stage 3 resulted in final re-equilibration at 0.5–0.4 GPa.

Recent work has shown that monazite-forming processes may involve not only reaction with other accessory phases but also with major silicate phases. Although production of population 5 monazite may have involved some consumption of earlier monazite and/or apatite, the strong textural and temporal correlation with silicate reactions requires assessment of the potential role of major phases. Monazite production during the progress of reaction (2) requires that rock-forming minerals other than garnet were the source of light rare earth elements (LREEs). Potential major silicate sources of phosphorous include garnet and feldspar. The analysis of Kohn & Malloy (2004) indicates that phosphorous is not likely to be a limiting factor in whether major silicate reactions can produce significant monazite. In this assemblage, feldspar appears to represent the only potentially significant major silicate source of LREEs (potential range from tens to hundreds of ppm according to Bea & Montero, 1999; Kretz *et al.*, 1999; Pyle & Spear, 1999; Kohn & Malloy, 2004). Therefore, breakdown of K-feldspar and syn-metamorphic dynamic recrystallization of matrix plagioclase could have provided a source of LREEs via a generalized reaction such as:

$$\mathrm{Grt} + \mathrm{Kfs} + \mathrm{Pl}_1 + \mathrm{H_2O} = \mathrm{Bt} + \mathrm{Sil} + \mathrm{Pl}_2 + \mathrm{Mzt} + \mathrm{Ap} \quad (4)$$

Pyle & Spear (2003) invoked a similar reaction in reverse to consume monazite during prograde metamorphism. Dissolution of earlier formed monazite and/or apatite is also possible. If our suggestion that feldspar was an important contributor of LREEs is true, then it would follow that the inevitable exhaustion of K-feldspar and cessation of matrix deformation could have contributed to the transition to xenotime growth, which is texturally linked to the product of reaction 3 and does not require significant amounts of LREEs. We suggest a generalized reaction for xenotime production in these rocks such as:

$$\mathrm{Grt} + \mathrm{Sil} + \mathrm{Qtz} \pm \mathrm{Mzt} \pm \mathrm{Ap} + \mathrm{H_2O} = \mathrm{Crd} + \mathrm{Xnt} \quad (5)$$

Legs Lake shear zone-related penetrative deformation in the felsic granulite must have ended during stage 3, as suggested by the relatively equant geometry of the Grt–Crd–Pl–Bt–Sil composite porphyroblasts in sample S32D. However, the composite porphyroblasts are stretched and disaggregated parallel to the extension direction in hydrous retrograde granulite that was subsequently overprinted by the younger Grease River shear zone (03M166B) (Figs 2d & 13a). Thus, Grease River shear zone deformation must have occurred after 1.85 Ga, which is consistent with previous geochronological data indicating *c.* 1.80 Ga deformation in the shear zone (Hanmer, 1997; Williams & Jercinovic, 2002).

Source of fluid influx in Legs Lake shear zone?

Major hydration and retrogression of the felsic granulite appears restricted to rocks within the Legs Lake shear zone. If so, this requires that the Legs Lake shear zone was a system open to channelized fluid influx and thus, a related question concerns the source of the externally derived fluid. Possible sources include water released from crystallizing intrusions such as the 1.85–1.80 Ga Hudsonian granite suite that was emplaced over much of the western Churchill province (Peterson *et al.*, 2002) or devolatilization reactions in Hearne domain metasedimentary rocks. We consider the first possibility to be unlikely because no 1.85 Ga intrusions have been recognized anywhere within the Legs Lake shear zone (Mahan *et al.*, 2003), although more distant sources may also be possible. However, prograde metamorphic reactions in Crd–Bt schist and amphibolite in the footwall Hearne domain are interpreted to have occurred synkinematically with respect to the Legs Lake shear zone (Mahan *et al.*, 2003). Therefore, devolatilizing reactions in the footwall are considered the most likely source of fluid that infiltrated into the hangingwall. This implies a general upward flow of fluid from the underthrust Hearne domain. It may be possible to test this hypothesis using oxygen isotopes if it can be demonstrated that alternative fluid sources should have isotopically distinct signatures that are also distinct from the originally anhydrous granulite.

CONCLUSIONS

The Legs Lake shear zone is a major crustal-scale feature that exerted structural control on hydrous fluid infiltration into dry high-*P* felsic granulite in the east Lake Athabasca region. The P–T–$M_{\mathrm{H_2O}}$ retrograde evolution of the granulite indicates that fluid influx into the hangingwall commenced at 0.8–0.7 GPa after an initial period of anhydrous decompression from 1.1 GPa. This marked the passage of deeper crust that was undergoing decompression over shallower crust that was being loaded. The shear zone acted as a mid-crustal channel for fluid that may have been produced by dehydration of metasediments in the underthrust Hearne domain. Synkinematic retrograde reactions initiated during the hydrated portion of the decompression history and consumed a considerable volume of garnet, which is recorded by distinctly high Y content in coeval monazite dated at 1853 ± 15 and 1851 ± 9 Ma in two respective samples. In contrast, high-*P* felsic granulite further removed from the active deformation zone preserves the peak assemblage and did not develop new Y-rich monazite. As a consequence, important details regarding the exhumation of this region were apparently only recorded within high strain zones that were active during the exhumation process.

We recognize five texturally, compositionally and temporally distinct populations of monazite in the

felsic granulite that record a long (> 600 Myr) and episodic tectonic history. Importantly, a major period of uplift of the high-*P* rocks is represented only by the fifth population, which also appears to be a relatively minor volumetric component. This population is restricted to rocks within the Legs Lake shear zone and correlates with major retrograde silicate reactions.

This study demonstrates the utility and necessity of integrating microstructural and petrological analysis with careful evaluation of the textural, compositional and age variation among monazite (and other accessory phases) in polymetamorphic terranes. The *in situ* nature and high spatial resolution of the microprobe were important because the fifth monazite population occurs only as thin (< 15 μm) discontinuous overgrowths. Similarly, the use of X-ray maps was essential for revealing and interpreting complex zoning patterns in individual grains. The results constrain an important part of the evolution of the Legs Lake shear zone and of the P–T–M_{H_2O}–time–deformation path and exhumation of high-*P* rocks in the east Lake Athabasca region. The data also provide important new insights into the relationships among accessory phase petrogenesis and hydrous fluid flow in ductile shear zones.

ACKNOWLEDGEMENTS

This research was funded in part by National Science Foundation grant EAR 0001152 to M.L. Williams and S. Bowring and by a GSA student research grant to K.H. Mahan. We thank R. Flowers, G. Dumond, S. Bowring, J. Baldwin and S. Hanmer (who collected the original S32D) for their insightful conversations. Thoughtful and constructive reviews by R. Berman and A. Möller are greatly appreciated. Thanks also to D. Robinson for handling the manuscript as editor-in-chief.

REFERENCES

Aspler, L. B. & Chiarenzelli, J. R., 1998. Two Neoarchean supercontinents? Evidence from the Paleoproterozoic. *Sedimentary Geology*, **120,** 75–104.

Baldwin, J. A., 2003. Petrological and geochronological constraints on the metamorphic evolution of high-pressure granulites and eclogites of the Snowbird tectonic zone, Canada. PhD Dissertation, Department of Earth, Atmospheric, and Planetary Sciences, Massachusetts Institute of Technology, Cambridge, MA, USA, 232 pp.

Baldwin, J. A., Bowring, S. A. & Williams, M. L., 2003. Petrologic and geochronologic constraints on high-pressure, high-temperature metamorphism in the Snowbird tectonic zone, Canada. *Journal of Metamorphic Geology*, **21,** 81–98.

Baldwin, J. A., Bowring, S. A., Williams, M. L. & Williams, I. S., 2004. Eclogites of the Snowbird tectonic zone: petrological and U–Pb geochronological evidence for Paleoproterozoic high-pressure metamorphism in the western Canadian Shield. *Contributions to Mineralogy and Petrology*, **147,** 528–548.

Baldwin, J. A., Bowring, S. A., Williams, M. L. & Mahan, K. H., 2006. Geochronological constraints on the evolution of high-pressure felsic granulites from an integrated electron microprobe and ID-TIMS geochemical study. *Lithos* DOI: 10.1016/j.lithos.2005.08.009.

Barnes, J. D., Selverstone, J. & Sharp, Z. D., 2004. Interactions between serpentinite devolatilization, metasomatism and strike–slip strain localization during deep-crustal shearing in the Eastern Alps. *Journal of Metamorphic Geology*, **22,** 283–300.

Bea, F. & Montero, P., 1999. Behavior of accessory phases and redistribution of Zr, REE, Y, Th, and U during metamorphism and partial melting of metapelites in the lower crust: an example from the Kinzigite Formation of Ivrea-Verbano, NW Italy. *Geochemica et Cosmochemica Acta*, **63,** 1133–1153.

Berman, R. G., 1991. Thermobarometry using multi-equilibrium calculations: a new technique, with petrological applications. *Canadian Mineralogist*, **29,** 833–855.

Berman, R. G., 1992. *Thermobarometry with Estimation of Equilibration State (TWEEQU): an IBM Compatible Software Package*. Geological Survey of Canada, Ottawa, Ontario.

Berman, R. G. & Aranovich, L. Ya., 1996. Optimized standard state and solution properties of minerals I. Model calibration for olivine, orthopyroxene, cordierite, garnet, and ilmenite in the system FeO–MgO–CaO–Al_2O_3–TiO_2–SiO_2. *Contributions to Mineralogy and Petrology*, **126,** 1–24.

Berman, R., Ryan, J. J., Tella, S. *et al.*, 2000. The case of multiple metamorphic events in the Western Churchill Province: evidence from linked thermobarometric and in-situ SHRIMP data, and jury deliberations. *Geological Association of Canada-Mineralogical Association of Canada Annual Meeting Abstracts*, Calgary, Alberta, Vol. 25, Conference CD, p. 836.

Berman, R. G., Davis, W. J., Aspler, L. B. & Chiarenzelli, J. R., 2002. *SHRIMP U–Pb Ages of Multiple Metamorphic Events in the Angikuni Lake Area, Western Churchill Province, Nunavut*. Geological Survey of Canada, Current Research, **2002-F3,** 9.

Berman, R. G., Sanborn-Barrie, M., Stern, R. A. & Carson, C. J., 2005. Tectonometamorphism at ca. 2.35 and 1.85 Ga in the Rae domain, western Churchill Province, Nunavut, Canada: insights from structural, metamorphic and in situ geochronological analysis of the southwestern Committee Bay Belt. *The Canadian Mineralogist*, **43,** 409–442.

Bingen, B. & van Breemen, O., 1998. U–Pb monazite ages in amphibolite- to granulite-facies orthogneiss reflect hydrous mineral breakdown reactions: Sveconorwegian Province of SW Norway. *Contributions to Mineralogy and Petrology*, **132,** 336–353.

Bucher, K. & Frey, M., 2002. *Petrogenesis of Metamorphic Rocks*, 7th edn. Springer-Verlag, Berlin.

Card, C. D., 2001. Basement rocks to the western Athabasca basin in Saskatchewan. *Saskatchewan Geological Survey, Summary of Investigations*, **2001–2,** 321–333.

Chapman, D. S. & Furlong, K. P., 1992. Thermal state of the continental lower crust. In: *Continental Lower Crust: Developments in Geotectonics*, Vol. 23 (eds Fountain, D. M., Arculus, R. & Kay, R. W.), pp. 179–199. Elsevier, Amsterdam.

Clark, C., Schmidt Mumm, A. & Faure, K., 2005. Timing and nature of fluid flow and alteration during Mesoproterozoic shear zone formation, Olary Domain, South Australia. *Journal of Metamorphic Geology*, **23,** 147–164.

Connolly, J. A. D., 1990. Calculation of multivariable phase diagrams: an algorithm based on generalized thermodynamics. *American Journal of Science*, **290,** 666–718.

Connolly, J. A. D. & Petrini, K., 2002. An automated strategy for calculation of phase diagram sections and retrieval of rock properties as a function of physical conditions. *Journal of Metamorphic Geology*, **20,** 697–708.

Etheridge, M. A., Wall, V. J. & Vernon, R. H., 1983. The role of the fluid phase during regional metamorphism and deformation. *Journal of Metamorphic Geology*, **1,** 205–226.

Evans, T. P., 2004. A method for calculating effective bulk composition modification due to crystal fractionation in garnet-bearing schist: implications for isopleth thermobarometry. *Journal of Metamorphic Geology*, **22,** 547–557.

Flowers, R. M., 2005. Stabilization, reactivation, and exhumation of cratonic lithosphere: a view from the lower crust, east Lake Athabasca area, western Canadian shield. PhD Dissertation, Massachusetts Institute of Technology, Cambridge, MA, USA.

Flowers, R. M., Bowring, S. A. & Williams, M. L., 2006. Timescales and intensities of high pressure metamorphism and anatexis, Snowbird Tectonic Zone, Canada. *Contributions to Mineralogy and Petrology*, in press.

Foster, G. & Parrish, R. R., 2003. Metamorphic monazite and the generation of *P–T–t* paths. *Geological Society Special Publication*, **220,** 25–47.

Foster, G., Kinny, P., Vance, D., Prince, C. & Harris, N., 2000. The significance of monazite U–Th–Pb age data in metamorphic assemblages; a combined study of monazite and garnet chronometry. *Earth and Planetary Science Letters*, **181,** 327–340.

Foster, G., Parrish, R. R., Horstwood, M. S. A., Chenery, S. & Gibson, H. D., 2004. The generation of prograde *P–T–t* points and paths; a textural, compositional, and chronological study of metamorphic monazite. *Earth and Planetary Science Letters*, **228,** 125–142.

Gibson, H. D., Carr, S. D., Brown, R. L. & Hamilton, M. A., 2004. Correlations between chemical and age domains in monazite, and metamorphic reactions involving major pelitic phases: an integration of ID-TIMS and SHRIMP geochronology with Y–Th–U X-ray mapping. *Chemical Geology*, **211,** 237–260.

Glazner, A. F. & Bartley, J. M., 1991. Volume loss, fluid flow and state of strain in extensional mylonites from the central Mojave Desert, California. *Journal of Structural Geology*, **13,** 587–594.

Goncalves, P., Nicollet, C. & Montel, J. M., 2004. Petrology and in-situ U–Th–Pb monazite geochronology of ultra-high temperature metamorphism from the Andriamena mafic unit, north-central Madagascar: significance of a petrographical PT path in a polymetamorphic context. *Journal of Petrology*, **10,** 1923–1957.

Gromet, L. P., 1991. Direct dating of deformational fabrics. In: *Applications of Radiogenic Isotope Systems to Problems in Geology, Short Course Handbook 19* (eds Heaman, L. & Ludden, J. N.), pp. 167–189. Mineralogical Society of Canada, Toronto.

Guiraud, M., Powell, R. & Rebay, G., 2001. H_2O in metamorphism and unexpected behavior in the preservation of metamorphic mineral assemblages. *Journal of Metamorphic Geology*, **19,** 445–454.

Hanmer, S., 1997. Geology of the Striding-Athabasca mylonite zone, northern Saskatchewan and southeastern District of Mackenzie, Northwest Territories. *Geological Survey of Canada*, **501,** 92p.

Hanmer, S., Parrish, R., Williams, M. L. & Kopf, C., 1994. Striding-Athabasca mylonite zone: complex Archean deep-crustal deformation in the East Athabasca mylonite triangle, N. Saskatchewan. *Canadian Journal of Earth Science*, **31,** 1287–1300.

Heaman, L. M., 1994. 2.45 Ga global mafic magmatism: Earth's oldest superplume? In: *Abstracts of the Eighth International Conference on Geochronology, Cosmochronology and Isotope Geology, Circular 1107* (eds Lauphere, M. A., Dalrymple, G. B. & Turrin, B. D.), p. 132.

Hermann, J. & Rubatto, D., 2003. Relating zircon and monazite domains to garnet growth zones: age and duration of granulite-facies metamorphism in the Val Malenco lower crust. *Journal of Metamorphic Geology*, **21,** 833–852.

Hoffman, P. F., 1988. United plates of America, the birth of a craton: Early Proterozoic assembly and growth of Laurentia. *Annual Review of Earth and Planetary Sciences*, **16,** 543–603.

Holland, T. & Powell, R., 1998. An internally consistent thermodynamic dataset for phases of petrological interest. *Journal of Metamorphic Geology*, **16,** 309–343.

Jercinovic, M. J. & Williams, M. L., 2005. Analytical perils (and progress) in electron microprobe trace element analysis applied to geochronology: background acquisition, interferences, and beam irradiation effects. *American Mineralogist*, **90,** 526–546.

Kohn, M. J. & Malloy, M. A., 2004. Formation of monazite via prograde metamorphic reactions among common silicates: implications for age determinations. *Geochimica et Cosmochimica Acta*, **68,** 101–113.

Kopf, C., 1999. Deformation, metamorphism, and magmatism in the East Athabasca mylonite triangle, northern Saskatchewan: implications for the Archean and Early Proterozoic crustal structure of the Canadian Shield. PhD Dissertation, Department of Geosciences, University of Massachusetts-Amherst, USA, 139 pp.

Kretz, R., 1983. Symbols for rock-forming minerals. *American Mineralogist*, **68,** 277–279.

Kretz, R., Campbell, J. L., Hoffman, E. L., Hartree, R. & Teesdale, W. J., 1999. Approaches to equilibrium in the distribution of trace elements among the principal minerals in a high-grade metamorphic terrane. *Journal of Metamorphic Geology*, **17,** 41–59.

Krikorian, L., 2002. Geology of the Wholdaia Lake segment of the Snowbird tectonic zone, Northwest Territories (Nunavut); a view of the deep crust during assembly and stabilization of the Laurentian craton. MSc Thesis, Department of Geosciences, University of Massachusetts-Amherst, Amherst, MA, USA, 90 pp.

Ludwig, K. R., 2003. *Isoplot/Ex Version 3.00: a Geochronological Toolkit for Microsoft Excel*. Berkeley Geochronology Center, Berkeley, CA.

Mahan, K. H. & Williams, M. L., 2005. Reconstruction of a large deep crustal exposure: implications for the Snowbird tectonic zone and early growth of Laurentia. *Geology*, **33,** 385–388.

Mahan, K. H., Williams, M. L. & Baldwin, J. A., 2003. Contractional uplift of deep crustal rocks along the Legs Lake shear zone, western Churchill Province, Canadian Shield. *Canadian Journal of Earth Sciences*, **40,** 1085–1110.

McFarlane, C. R. M., Connelly, J. N. & Carlson, W. D., 2005. Monazite and xenotime petrogenesis in the contact aureole of the Makhavinekh Lake Pluton, northern Labrador. *Contributions to Mineralogy and Petrology*, **148,** 524–541.

Möller, A., O'Brien, P. J., Kennedy, A. & Kröner, A., 2003. Linking growth episodes of zircon and metamorphic textures to zircon chemistry: an example from the ultrahigh-temperature granulites of Rogaland (SW Norway). In: *Geochronology: Linking the Isotopic Record with Petrology and Textures* (eds Vance, D., Müller, W. & Villa, I. M.), *Special Publications, Journal of the Geological Society of London*, **220,** 65–81.

Montel, J. M., Foret, S., Veschambre, M., Nicollet, C. & Provost, A., 1996. Electron microprobe dating of monazite. *Chemical Geology*, **131,** 37–53.

Oliver, N. H. S., 1996. Review and classification of structural controls on fluid flow during regional metamorphism. *Journal of Metamorphic Geology*, **14,** 477–492.

Otamendi, J. E., de la Rosa, J. D., Patiño Douce, A. E. & Castro, A., 2002. Rayleigh fractionation of heavy rare earths and yttrium during metamorphic garnet growth. *Geology*, **30,** 159–162.

Pan, Y., 1997. Zircon and monazite forming metamorphic reactions at Manitouwadge, Ontario. *Canadian Mineralogist*, **35,** 105–118.

Paquette, J. L., Goncalves, P., Nicollet, C. & Devouard, B., 2004. Micro-drilling ID-TIMS U–Pb dating of single monazites: a new method to unravel complex poly-metamorphic evolutions: application to the UHT granulites of Andriamena (North-Central Madagascar). *Contributions to Mineralogy and Petrology*, **147,** 110–122.

Parrish, R. R., 1990. U–Pb dating of monazite and its application to geological problems. *Canadian Journal of Earth Sciences*, **27,** 1431–1450.

Peterson, T. D., van Breemen, O., Sandeman, H. A. & Cousens, B., 2002. Proterozoic (1.85–1.75 Ga) igneous suites of the western Churchill Province: granitoid and ultrapotassic magmatism in a reworked Archean hinterland. *Precambrian Research*, **119,** 73–100.

Powell, R. & Holland, T., 1994. Optimal geothermometry and geobarometry. *American Mineralogist*, **79,** 120–133.

Pyle, J. M. & Spear, F. S., 1999. Yttrium zoning in garnet: coupling of major and accessory phases during metamorphic reactions. *Geological Materials Research*, **1,** 1–49.

Pyle, J. M. & Spear, F. S., 2000. An empirical garnet (YAG)-xenotime thermometer. *Contributions to Mineralogy and Petrology*, **138,** 51–58.

Pyle, J. M. & Spear, F. S., 2003. Four generations of accessory-phase growth in low-pressure migmatites from SW New Hampshire. *American Mineralogist*, **88,** 338–351.

Pyle, J. M., Spear, F. S. & Wark, D. A., 2002. Electron microprobe analysis of REE in apatite, monazite, and xenotime: protocols and pitfalls. *Reviews in Mineralogy and Geochemistry*, **48,** 337–362.

Pyle, J. M., Spear, F. S., Wark, D. A., Daniel, C. G. & Storm, L. C., 2005. Contributions to precision and accuracy of monazite microprobe ages. *American Mineralogist*, **90,** 547–577.

Rayner, N. M., Stern, R. A. & Rainbird, R. H., 2003. SHRIMP U–Pb detrital zircon geochronology of Athabasc Group sandstones, northern Saskatchewan and Alberta. *Current Research*, **2003-F2,** 22.

Selverstone, J., Morteani, G. & Staude, J.-M., 1991. Fluid channelling during ductile shearing: transformation of granodiorite into aluminous schist in the Tauern Window, Eastern Alps. *Journal of Metamorphic Geology*, **9,** 419–431.

Slimmon, W. L., 1989. *Compilation Bedrock Geology Map Series, Fond-du-Lac NTS Area 74O*. Saskatchewan Energy and Mines. 1:250000, Report 247, Map 247A.

Snoeyenbos, D. R., Williams, M. L. & Hanmer, S., 1995. An Archean eclogite facies terrane in the western Canadian Shield. *European Journal of Mineralogy*, **7,** 1251–1272.

Spear, F. S., 1993. *Metamorphic Phase Equilibria and Pressure–Temperature–time paths*, 2nd edn. Mineralogical Society of America, Washington, DC.

Spear, F. S. & Pyle, J. M., 2002. Apatite, monazite, and xenotime in metamorphic rocks. *Reviews in Mineralogy & Geochemistry*, **48,** 293–331.

Stern, R. A. & Berman, R. G., 2000. Monazite U–Pb and Th–Pb geochronology by ion microprobe, with an application to in situ dating of an Archean metasedimentary rock. *Chemical Geology*, **172,** 113–130.

Suzuki, K., Adachi, M., & Tanaka, T., 1991. Middle Precambrian provenance of Jurassic sandstone in the Mino Terrane, central Japan: Th–U–total Pb evidence from an electron microprobe monazite study. *Sedimentary Geology*, **75,** 141–147.

Vernon, R. H., 1976. *Metamorphic Processes: Reactions and Microstructure Development*. George Allen & Unwin Ltd, London.

Vielzeuf, D. & Schmidt, M. W., 2001. Melting relations in hydrous systems revisited; application to metapelites, metagreywackes and metabasalts. *Contributions to Mineralogy and Petrology*, **141,** 251–267.

Williams, M. L. & Hanmer, S., 2005. Structural and metamorphic processes in the lower crust: evidence from the East Athabasca mylonite triangle, Canada, a deep-crustal isobarically cooled terrane. In: *Evolution and Differentiation of the Continental Crust* (eds Brown, M. & Rushmer, T.), pp. 232–268. Cambridge University Press, Cambridge.

Williams, M. L. & Jercinovic, M. J., 2002. Microprobe monazite geochronology: putting absolute time into microstructural analysis. *Journal of Structural Geology*, **24,** 1013–1028.

Williams, M. L., Hanmer, S., Kopf, C. & Darrach, M., 1995. Syntectonic generation and segregation of tonalitic melts from amphibolite dykes in the lower crust, Striding-Athabasca mylonite zone, Northern Sastachewan. *Journal of Geophysical Research*, **100,** 15717–15734.

Williams, M. L., Melis, E. A., Kopf, C. & Hanmer, S., 2000. Microstructural tectonometamorphic processes and the development of gneissic layering: a mechanism for metamorphic segregation. *Journal of Metamorphic Geology*, **18,** 41–57.

Williams, M. L., Jercinovic, M. J., Goncalves, P. & Mahan, K. H., 2006. Format and philosophy for collecting, compiling, and reporting microprobe monazite ages. *Chemical Geology*, **225,** 1–15.

Wing, B. A., Ferry, J. M. & Harrison, T. M., 2003. Prograde destruction and formation of monazite and allanite during contact and regional metamorphism of pelites: petrology and geochronology. *Contributions to Mineralogy and Petrology*, **145,** 228–250.

Yang, P. & Rivers, T., 2002. The origin of Mn and Y annuli in garnet and the thermal dependence of P in garnet and Y in apatite in calc-pelite and pelite, Gagnon Terrane, western Labrador. *Geological Materials Research*, **4-1**.

Yund, R. A. & Tullis, J., 1991. Compositional changes of minerals associated with dynamic recrystallization. *Contributions to Mineralogy and Petrology*, **108,** 346–355.

Received 30 June 2005; revision accepted 10 January 2006.